Monthly Notices of the ROYAL ASTRONOMICAL SOCIETY

MNRAS **532,** 1929–1947 (2024) https://doi.org/10.1093/mnras/stae1498
Advance Access publication 2024 July 12

Simulations of pulsed overpressure jets: formation of bellows and ripples in galactic environments

Carl Richards[1]★ and Michael D. Smith[1,2]

[1]*Centre for Astrophysics & Planetary Science, The University of Kent, Canterbury, Kent CT2 7NH, UK*
[2]*Department of Physics, Amrita School of Physical Sciences, Amrita Vishwa Vidyapeetham, Amritapuri Campus, Kollam, Kerala, 690525, India*

Accepted 2024 June 13. Received 2024 June 12; in original form 2024 February 3

ABSTRACT

Jets from active nuclei may supply the heating which moderates cooling and accretion from the circum-galactic medium. While steady overpressured jets can drive a circulatory flow, lateral energy transfer rarely exceeds 3 per cent of jet power, after the initial bow shock has advanced. Here, we explore if pulses in high-pressure jets are capable of sufficient lateral energy transfer into the surrounding environment. We answer this by performing a systematic survey of numerical simulations in an axisymmetric hydrodynamic mode. Velocity pulses along low Mach jets are studied at various overpressures. We consider combinations of jet velocity pulse amplitude and frequency. We find three flow types corresponding to slow, intermediate, and fast pulsations. Rapid pulsations in light jets generate a series of travelling shocks in the jet. They also create ripples which propagate into the ambient medium while a slow convection flow brings in ambient gas which is expelled along the jet direction. Long period pulses produce slowly evolving patterns which have little external effect, while screeching persists as in non-pulsed jets. In addition, rapid pulses in jets denser than the ambient medium generate a novel breathing cavity analogous to a lung. Intermediate period pulses generate a series of bows via a bellows action which transfer energy into the ambient gas, reaching power efficiencies of over 30 per cent when the jet overpressure is sufficiently large. This may adequately inhibit galaxy gas accretion. In addition, such pulses enhance the axial out-flow of jet material, potentially polluting the circum-galactic gas with metal-enriched interstellar gas.

Key words: hydrodynamics – methods: numerical – galaxies: jets.

1 INTRODUCTION

Galaxies evolve under the influence of gas flows between their interstellar medium and their surrounding gaseous haloes, known as the circum-galactic medium (CGM). Though the CGM is substantially less dense than its associated galaxy's interstellar medium, this vast reservoir harbours 3–5 times as many baryons and heavy elements (Peeples et al. 2019). However, estimated star-formation rates in many galaxies are lower than expected given the anticipated surrounding ambient cool-gas inflows (Ishibashi & Fabian 2012). Although the jets from active galactic nuclei (AGN) are not well understood, it may be possible for energy transfer from the gas jets of AGN to heat the ambient surrounding the host galaxy and moderate these inflows (e.g. Ishibashi & Fabian 2012; Bambic & Reynolds 2019).

The initial advance of jets of high pressure, as well as pressure-matched jets, have been studied through numerical simulations (Gómez et al. 1997; Martí, Perucho & Gómez 2016; Moya-Torregrosa et al. 2021). In general, the impacting jet drives a bow shock into the ambient medium which can release up to 70 per cent of the jet power into heating the environment (Hardcastle & Krause 2013; Bourne & Sijacki 2021; Huško & Lacey 2023), reaching even higher values at low-jet densities (Donohoe & Smith 2016) and relativistic jet speeds (Perucho, Quilis & Martí 2011). Prasad, Voit & O'Shea (2022) show that reducing the jet opening angle increases the jet momentum flux, enabling it to drill through to larger radii without effectively coupling with the CGM. However, once the bow has vacated the near field of the nozzle, the energy transfer is small. One way to ameliorate this, could be by considering start–stop or episodic jets with millions of years in between outbursts (Chavan, Dabhade & Saikia 2023).

Significant shock configurations in supersonic jets are found in overpressure jets, i.e. where the jet/ambient pressure ratio is >1. Overpressure jets produce shock fronts, which are locations of rapid changes in temperature, pressure, and density, and where post-shock gas acceleration occurs. Low Mach steady-state jets generally drive a circulatory motion in which the ambient medium is driven out along the jet axial direction, while mass and energy from the surrounding ambient flow laterally inwards to back-fill. Once the initial bow shock has propagated out, the noise from the jet, i.e. sound pressure waves, is insufficient to significantly alter the environment. A maximum lateral power output from sound waves, caused by jet shock front oscillations about a mean shock location, is calculated to be 3 per cent of jet power (Smith & Keogh 2022).

As a step to determine if overpressured jets which are pulsed can regulate the environment, we first studied jets of constant speed. Smith & Keogh (2022) used the code *PLUTO* in the 2D axisymmetric

★ E-mail: cr704@kent.ac.uk

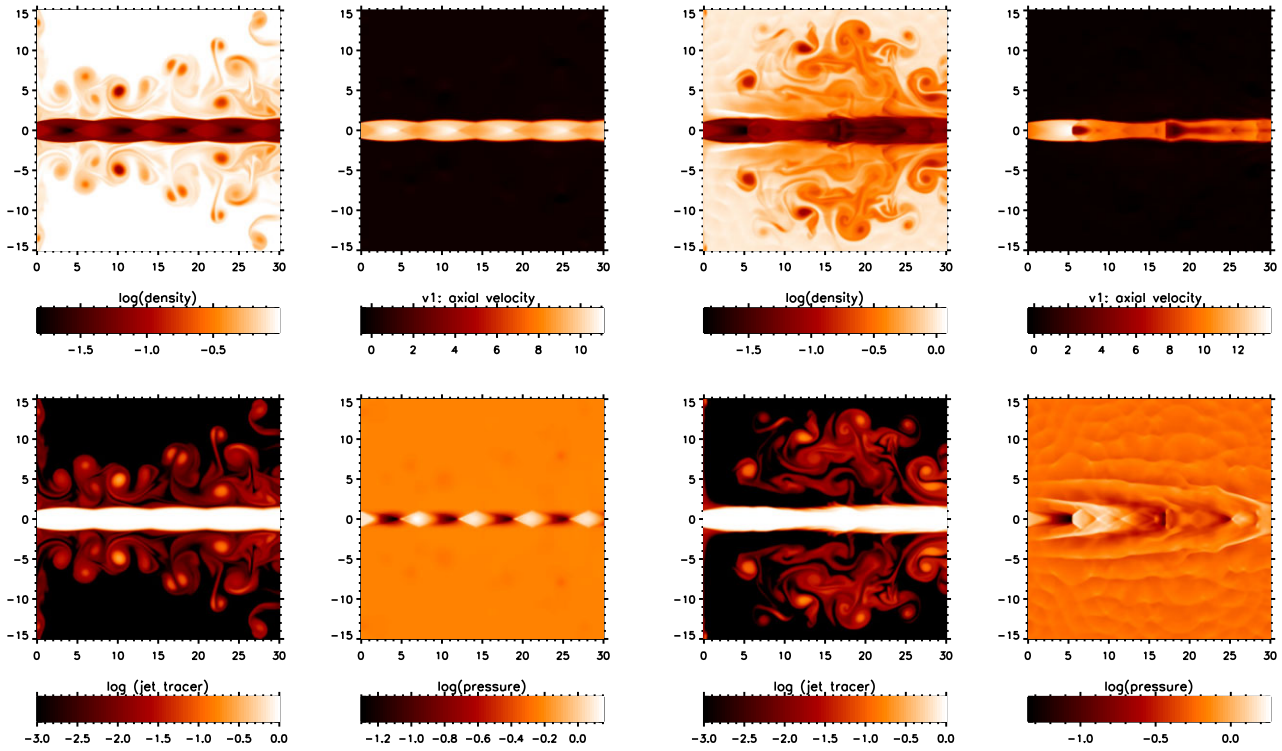

Figure 1. Effect of rapid pulsations on a light jet with low overpressure. A light ($\eta = 0.1$) Mach 2 jet with low overpressure ($\kappa = 2$) is considered, with comparison of physical parameters for the constant inflow jet (left panels) to the rapidly pulsed jet (right panels). Note the oblique shocks established on the left. The imposed sinusoidal velocity pulses on the right are of amplitude 40 per cent and period 2. These are cross-sectional snapshots at time 200, the end of the simulation period.

hydrodynamic configuration where a survey was carried out of low Mach (Mach 2) underexpanded (overpressure) steady-state jets. Smith & Richards (2023) carried out similar systematic simulations for high Mach jets (up to Mach 8). They identified conditions which generally generate Mach shock discs rather than oblique regular shock reflections and explored other potential observational diagnostics, including the disc size, distance from the nozzle, and oscillations in shock positions. The overpressure jets contribute to lateral sound wave generation through screeching, but insufficient to regulate galaxy formation. Unlike low Mach number jets which tend to advect ambient gas along the jet-axis, this effect was largely absent for higher Mach jets.

Overpressured jets are important shock generators that can be particularly relevant in the vicinity of astrophysical objects, where the jets propagate away from the cores that harbour protostars or supermassive black holes. As a jet exits from the core, the steep negative pressure gradient in the ambient medium (Smith 1982; Porth & Komissarov 2015) leaves the jet pressure relatively high at the effective exit of the core.

The over-pressured jet expands as it exits the nozzle. The pressure near the jet boundary falls to the value of the ambient medium. The pressure gradient is reversed, via a shock, and the diverging jet then converges. However, the pressure on the jet axis continues to fall oblivious of the jet boundary pressure. Another shock front is then necessary near the axis in order to raise the thermal pressure i.e. via a weak oblique/regular reflection shock, also referred to as a diamond shock. The result is a repeated diverging–converging shock pattern which drives recollimation shocks into the jet (Powell 1953). A distinctive flow channel is cut with little further disturbance to the immediate environment. At high overpressures, the oblique shocks fail to raise the axial pressure and a strong detached Normal shock or Mach disc is formed. An example of a jet with weak oblique/regular reflection shocks can be found in Fig. 1 (left panel), and of a jet with strong Normal/Mach Disc shocks can be found in Fig. 2 (left panel). This delay in communication between the jet surface and axis causes a hysteresis effect that can also cause oscillatory instabilities through positive feedback.

We consider velocity pulses superimposed on four significantly different steady-state Mach 2 jets, covering a wide range of key parameters. For each, we take a range of pulse frequencies and amplitudes. The chosen parameters are based upon judgements using relevant characteristic jet time-scales. Observational evidence however is limited, e.g. the quasi-stationary shocks associated with jets, such as the protostellar jet HH154 (Favata et al. 2006) are proposed to be a diamond shock (Bonito et al. 2011), and a fraction of observed blazars (Weaver et al. 2022), however, there is insufficient data to constrain individual jet properties.

To study the energy transfer, we build upon (Smith & Keogh 2022), taking two-dimensional axisymmetric hydrodynamics for Mach 2 jets. They found at low overpressures, steady flows with a sustained diamond shock pattern were produced in which little energy is transmitted laterally. At moderate and high overpressures, a stationary flow pattern is not achieved. Here, Mach shock disc oscillations are able to send sound waves into the ambient medium at a level of a few per cent at most.

This raises the question of the type of imposed pulsations which would significantly disturb the environment. We select a low- and a high-jet/ambient overpressure. These pressure ratios cover the two contrasting shock patterns of diamond or reflective oblique shocks and Mach shock reflection discs, respectively. We then superimpose

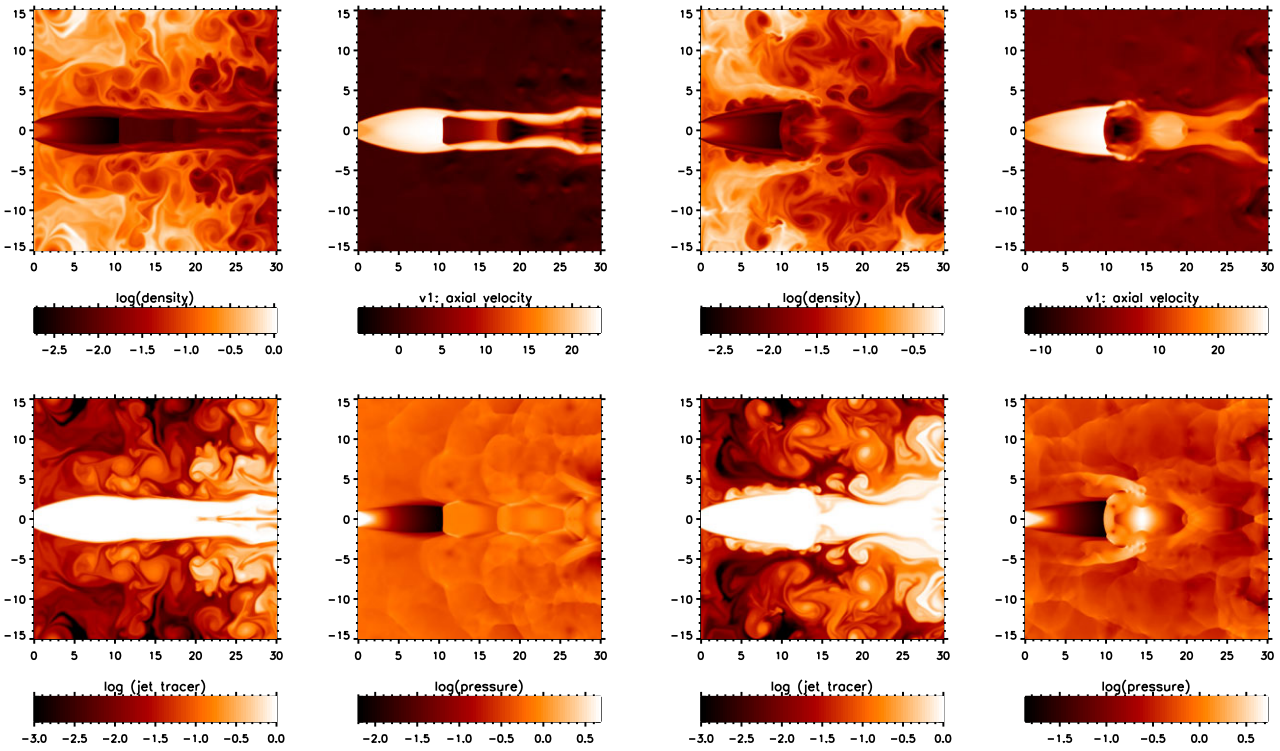

Figure 2. Effect of rapid pulsations on a light jet with high overpressure. A light ($\eta = 0.1$) Mach 2 jet with high overpressure $\kappa = 8$ is considered, with comparison of physical parameters for the constant inflow jet (left panels) to the rapidly pulsed jet (right panels). The imposed sinusoidal velocity pulses on the right are of amplitude 40 per cent and period 2. These are cross-sectional snapshots at time 200.

sinusoidal variations in velocity of different amplitudes and periods. By covering time-scales which are measured relative to the time for jet flow to reach the first shock, i.e. stand-off shock, and the time for a flow pattern to settle, related to the Kelvin–Helmholtz wave speed, we should uncover diverse dynamic phenomena.

Additional physics will allow more specific conclusions. For example, relativistic motions and magnetic fields are excluded here. These have been investigated for the case of steady jets with low overpressures by Martí et al. (2016). Also, a realistic CGM is non-uniform and may contain long-lived vortices on small scales, and may also develop significant pressure variations. However, here we begin each simulation with a uniform ambient density.

In this paper, Section 2 describes our method, Section 3 explains the analysis tools used, Section 4 presents results of pulse simulations, and Section 5 examines energy and mass distributions. In Section 6, we discuss the results and in Section 7 our conclusions.

2 METHOD

2.1 Simulation set-up

We simulate hydrodynamic supersonic jets injected with a jet/ambient thermal overpressure ratio into a uniform medium. The flow is inviscid except where high gradients occur along interfaces, slip-lines and shock fronts. The circular jets consist of a uniform adiabatic gas that is inserted on the boundary of a cylindrical computational grid. We assume 2D cylindrical symmetry which may be justified close to the orifice while the growth of surface instabilities remains small.

A large surrounding reservoir of uniform pressure and density is taken to avoid artificial boundary issues. The initial impact on to the grid, followed by the oscillations in the flow patterns and the imposed velocity pulsations will cause a pressure rise. The result can be a gradual build-up in the ambient pressure. To enable the pressure to be relieved within the limited computational domain, a large constant pressure reservoir surrounds the displayed grids, both radially and axially. This is achieved with little computing cost by the addition of staggered grids out to large physical distances. In this way we aim to maintain a free environment that is sufficiently large so that disturbances are not trapped close to the jet.

The jet is launched with a ramp up of the jet speed from zero to the final speed over ten ambient medium sound jet-radius crossing-times (the standardized units of time). Different ramp times and physical sizes were tested in order to check that initial and boundary conditions did not influence the final flow pattern at 200 time-units. Tests have shown that the choice of between zero and 40 sound crossing times for the ramp time has no effect on the flow pattern by 100 time-steps (half the simulation duration) (Smith & Keogh 2022).

The simulations were performed with *PLUTO*, a grid-based code, incorporating Godunov-type shock-capturing schemes, which is freelydistributed (Mignone et al. 2007).[1] After comparing the results of numerous options, we chose a fast linear interpolation time-stepping Riemann solver as developed by Harten, Lax and Van Leer and detailed by Toro, Spruce & Speares (1994). However, for some simulations use of the Ausmchar Riemann Solver was necessary, to avoid numerical errors (negative pressures). The Hancock time-stepping Courant Friedrichs Lewy number was taken as 0.4.

We adapt the code initial and boundary conditions as follows: reflection conditions are imposed on the plane from which the circular parallel jet flow exits and on the jet symmetry axis. Free outflow

[1] http://plutocode.ph.unito.it/

conditions are imposed on the other grid boundaries. The subsequent post-processing was performed with algorithms incorporated into IDL software.

Five properties are recorded to file at each of 1000 data cashes, separated by 0.2 time-units, allowing evolution over 200 time-units. The parameters are the density, ρ, pressure, p, two velocity components, v_z (axial velocity) and v_r (radial or lateral velocity), and a mass-weighted jet tracer, χ.

2.2 Parameters and dimensions

The general configuration follows previous work on the steady release of gas from circular nozzles at Mach 2 (Smith & Keogh 2022). The following normalized units allow for ease of scaling. The jet radius is set to $R_{\rm jet} = 1$. By setting the ambient sound speed also to one, i.e. $c_{\rm amb} = 1$, the unit of time, given as the jet radius crossing time at the local speed of sound, is $R_{\rm jet}/c_{\rm amb} = 1$.

The specific heat ratio which yields the adiabatic index is taken as $\gamma = 5/3$, appropriate where a gas behaves with three degrees of freedom (monatomic gas). We complete the set of independent variables by setting the ambient density to $\rho_{\rm amb} = 1$.

We consider ranges in jet/ambient overpressure and density ratios between the two media, designated as $\kappa = p_{\rm jet}/p_{\rm amb}$ and $\eta = \rho_{\rm jet}/\rho_{\rm amb}$, respectively.

The sound speed,

$$c_{\rm amb} = \sqrt{\frac{\gamma \cdot p_{\rm amb}}{\rho_{\rm amb}}}, \tag{1}$$

yields a pressure $p_{\rm amb} = 1/\gamma = 0.6$ and internal energy per unit volume $u_{\rm amb} = p_{\rm amb}/(\gamma - 1) = 0.9$.

We fix the initial jet speed $v_{\rm o}$ and Mach number, $M_{\rm o}$, so that $v_{\rm o} = M_{\rm o} c_{\rm jet}$ where $c_{\rm jet}^2 = \kappa/\eta$. Note that higher density jets have lower absolute speeds compared to lower density jets for the same Mach number, and therefore tend to have lower jet powers, and be less turbulent.

The inner uniform cylindrical grids consist of 200 radially distributed zones and 400 axial zones. This converts into 15 $R_{\rm jet}$ and $15M_{\rm o} \times R_{\rm jet}$, respectively. We then display cross-sections through an entire computational cylinder as shown in Figs 1 and 2.

To avoid edge effects, we extend the computational domain to $65R_{\rm jet}$ and $(15M_{\rm o} + 100) \times R_{\rm jet}$ in the radial and axial directions, respectively. This is achieved by adding 100 and 200 zones on standard format geometrically staggered grids on to the uniform section. Reflection boundary conditions are applied to the axis and the plane/surface containing the jet nozzle.

2.3 Constant speed inflow parameters

Combinations of the parameters which provide the basis for the analysis are summarizsed in Tables 1 and 2.

Jets with high overpressures have received some attention in the astrophysical context. Mizuno et al. (2015) explored the near-field of relativistic magnetohydrodynamic jets, but limited to the steady low overpressure of $\kappa = 1.5$. Martí (2015) also studied steady relativistic jets, with rotation, up to $\kappa = 5$. We have chosen two overpressures which encapsulate the two major shock patterns for a Mach number of 2, $\kappa = 2$ for regular shock reflection, and $\kappa = 8$ for a prominent Mach shock disc. Smith & Keogh (2022) found, for Mach 2 jets, that oblique/reflection shocks, creating diamond shock patterns, were found for $\kappa < 3.5$, while strong detached normal shocks (Mach discs) become established at greater overpressure ratios.

Table 1. Chosen parameters which define the constant-inflow simulations (top) and the pulsed simulations (bottom).

Steady-state/constant inflow jet parameters				
$M_{\rm o}$ (Mach No) = 2				
R (Initial jet ramp up) = 10 time-units				
$K = \kappa$		$E = \eta$		
(Jet/ambient pressure ratio)		(Jet/ambient density ratio)		
2	8	0.1	10	
Pulse jet parameters				
P = period (time-units)		velocity pulse amplitude/v_o, $f_{\rm pulse}$		
2	10	40	0.4	1.0

Table 2. Subset of Mach 2 steady-state and pulsed jet simulations presented in this paper.

Figure number	Pressure ratio κ	Density ratio η	Pulse period	Velocity $V_{\rm max}/v_o$
1(left)	2	0.1	–	–
1(right)	2	0.1	2	1.4
2(left)	8	0.1	–	–
2(right)	8	0.1	2	1.4
3	2	0.1	–	–
4	2	0.1	2	1.4
5(left)	2	0.1	–	–
5(right)	2	0.1	2	1.4
6(left)	8	0.1	–	–
6(right)	8	0.1	2	1.4
7	8	0.1	2	1.4
8(left)	8	10	–	–
8(right)	8	10	2	1.4
9	8	10	2	1.4
10 (left)	8	10	–	–
10(right)	8	10	2	1.4
11 (left)	2	0.1	10	2.0
11 (right)	8	10	10	2.0
12	2	0.1	10	2.0
13	8	10	10	2.0
14(left)	3.5	0.1	–	–
14(right)	3.5	0.1	40	2.0
15	3.5	0.1	40	2.0
16	3.5	0.1	2, 10, 40	2.0
17	2	10	10	1.4
18	2, 8	0.1	1–100	2.0
19	2 – 3.5 – 4 – 6 – 8	0.1	2 – 10 – 40	2.0
20	2, 8	0.1	1–100	2.0
21 (upper)	2	10	10	1.4
21 (lower)	8	0.1	10	2.0

A summary of the four constant-inflow/steady-state base-jet parameters is provided in Table 1, together with nomenclature used. The jets are denoted as M2K2E0.1R10 (Fig. 1, left panel), M2K8E0.1R10 (Fig. 2, left panel), M2K8E10R10 (Fig. 8, left panel), and M2K2E10R10 (note that both high overpressure jets are similar, with the heavy jets less energetic and less turbulent).

2.4 Pulse periods and amplitudes

Jet variations could manifest themselves in many forms at the nozzle, e.g. involving velocity, pressure, density and/or opening angle, in the simplest forms. Here, we limit the variations to the form of velocity fluctuations.

We superimpose sinusoidal time variations on to the uniform velocity with a frequency ω. Holding the pressure and density constant, this is equivalent to varying the Mach number. The pulses are applied throughout the simulation. This yields:

$$v_{\rm jet}(t) = v_{\rm o}(1 + f_{\rm pulse}\sin\omega t). \quad (2)$$

The flow dynamical time-scale, $t_{\rm D}$, is crucial when choosing the pulse period $P = 2\pi/\omega$. Here, the time-scale is given by the jet speed and distance to the stand-off shock, i.e. the first shock, where the jet first converges on to the jet flow axis, for oblique/regular reflection shocks, or where the first Mach disc is established, using equations from Smith & Keogh (2022).

Having chosen two overpressures which encapsulate the two major shock patterns for a Mach number of 2, we determined pulse periods which should distinguish different jet dynamical effects.

For Mach 2 jets with $\kappa < 3.5$, regular reflection is rapidly established. Hence, for low κ, we use the stand-off distance for regular reflection (also referred to as shock diamonds),

$$D_1 = \sqrt{(M_{\rm o}^2 - 1)}\kappa^{\beta} R_{\rm jet}, \quad (3)$$

with $\beta = 1.2$ and the initial jet speed $v_{\rm o}$, to yield the dynamical time

$$t_{D1} = \frac{D_1}{v_{\rm o}} = \sqrt{(1 - 1/M_{\rm o}^2)}\kappa^{0.7}\sqrt{\eta}, \quad (4)$$

in units of $R_{\rm jet}/c_{\rm amb}$.

For high κ, with $\kappa > 3.5$, when Mach discs are prevalent, we use the formula for Mach shock discs,

$$D_2 = 1.38\gamma^{1/2}\kappa^{1/2}M_{\rm o}R_{\rm jet}. \quad (5)$$

to yield the value

$$t_{D2} = \frac{D_2}{v_{\rm jet}} = 1.38\sqrt{(\gamma\eta)}, \quad (6)$$

again in units of $R_{\rm jet}/c_{\rm amb}$.

Substituting $\kappa = 2$ into these formulae, we find $t_{D1} = 0.48$ for $\eta = 0.1$ and $t_{D1} = 4.75$ for $\eta = 10$.

Substituting $\kappa = 8$, into these formulae, we find $t_{D2} = 0.56$ for $\eta = 0.1$ and $t_{D2} = 5.65$ for $\eta = 10$.

While the dynamical time motivates our choice of pulse periods, the time-scale for the channel to change shape is equally important. This second time-scale is the time for Kelvin–Helmholtz surface waves moving in the flow direction to traverse from the nozzle to the stand-off shock. This wave speed corresponds to that of surface waves in response to the changing component of ram pressure pushing against the jet-ambient interface. We can thus approximate the time-scale by taking the maximum Kelvin–Helmholtz wave speed as an indicator, as determined in appendix A of Smith & Keogh (2022);

$$V_{KH} = M_{\rm o}\frac{\sqrt{\kappa}}{1 + \sqrt{\eta}}. \quad (7)$$

The corresponding time-scale is fixed by the stand-off distances stated above. Taken together, this yields

$$t_{KH,1} = \frac{D_1}{V_{KH}} = \sqrt{(1 - 1/M^2)}\kappa^{\beta-1/2}(1 + \sqrt{\eta}) \quad (8)$$

for regular reflection, and

$$t_{KH,2} = \frac{D_2}{V_{KH}} = 1.38\sqrt{\gamma}\ \ (1 + \sqrt{\eta}), \quad (9)$$

independent of the pressure for Mach shock discs.

Substituting $\kappa = 2$ into these formulae, we find $t_{KH,1} = 3.96$ for $\eta = 0.1$ and $t_{KH,1} = 12.5$ for $\eta = 10$.

Substituting $\kappa = 8$ into these formulae, we find $t_{KH,2} = 4.72$ for $\eta = 0.1$ and $t_{KH,2} = 14.9$ for $\eta = 10$.

The expedient conclusion is that the time-scales are not sensitive to the value of the overpressure, κ. Approximately, for light jets the dynamical time is 0.5 and the surface-wave time is 4. While for heavy jets, the dynamical time is 5 and the surface-wave time is 15. Based upon these times, we have thus chosen fiducial periods of 2, 10, and 40, essentially short-, medium-, and long-pulse period durations.

Two velocity amplitudes were covered in detail. A sinusoidal variation with amplitude $f_{\rm pulse}$ and assigned period were superimposed. First a maximum sinusoidal value of 100 per cent velocity i.e. a velocity cycle between zero and 2.0× steady-state Mach speed (denoted V2.0), i.e. essentially a restarting jet, and also an intermediate velocity amplitude, in this case a value of 40 per cent was chosen i.e. a velocity cycle between 0.6 and 1.4 $\times v_{\rm o}$ (denoted V1.4).

3 ANALYSIS TOOLS

Given the adiabatic condition, if a steady flow pattern were established, the mass momentum and energy fluxes through cross-sections of the flow should be conserved (Smith & Keogh 2022). Hence, to analyse the pulsed simulations, we calculate these three quantities where the momentum flux is in terms of ram and thermal pressure and the power is the combination of enthalpy and kinetic energy. The vast ambient reservoir can resupply gas ejected due to the initial jet impulse and later jet oscillations.

The mass flux injected on to the domain is

$$\dot{\mathcal{M}}_{\rm jet} = \rho_{\rm jet}\cdot v_{\rm jet}\cdot A, \quad (10)$$

where $A = (1 - \mu)\pi R_{\rm jet}^2$ is the jet area. Here, μ represents a small adjustment since the numerical nozzle profile is an approximation to a circle of radius $R_{\rm jet}$. In terms of the scaling:

$\dot{\mathcal{M}}_{\rm jet} = (1 - \mu)\pi(\kappa\eta)^{1/2}M$.

The momentum flow rate on to the grid is

$$\dot{\mathcal{P}}_{\rm jet} = (\rho_{\rm jet}\cdot v_{\rm jet}^2 + p_{\rm jet})\cdot A. \quad (11)$$

This can be written in the form

$$\dot{\mathcal{P}}_{\rm jet} = (1 - \mu)\pi\kappa(M^2 + 1/\gamma). \quad (12)$$

Finally, the energy flux has two components: the kinetic flux and the enthalpy flux which in turn consists of the internal energy and the work done, $p\mathcal{V}$, where $\mathcal{V} = 1/\rho$ is the specific volume. On dividing through by the mass conservation relation, this simplifies to Bernoulli's equation with the Bernoulli constant, U given by;

$$\mathrm{U}^2 = v_{\rm jet}^2 + \frac{2\gamma}{\gamma - 1}\frac{p_{\rm jet}}{\rho_{\rm jet}}. \quad (13)$$

Therefore, the total available power entering the domain is $\dot{\mathcal{M}}_{\rm jet}\mathrm{U}^2/2$. We can also follow the equivalent quantities downstream to understand how energy is exchanged between forms and media (Donohoe & Smith 2016).

We present below four-panelled colour-scale diagrams to display distributions of the physical parameters in the axial–radial (z –r) plane which show the density, axial velocity, jet tracer, and pressure. The jet tracer is mass weighted with a value of one for the material originating from the jet, and zero for the ambient gas.

Space–time diagrams of the pressure are employed to analyse the temporal changes due to the pulses. These illustrate the propagation of energy pulses along the jet axis.

Last, but not least, movies provide an additional analysis tool to better understand flow patterns and have also been essential to see

off-axis effects, as well as giving an overall perspective of the jet dynamics. The movies produced also include movie-graphs, which provide a dynamic quantitative perspective.

4 RESULTS

We systematically explore a range of parameters. We chose three pulsation periods, two amplitudes, two overpressure ratios, and two density ratios to yield 24 simulations. With the inclusion of the four constant inflow simulations, the steady-state base-jets, a total of 28 runs were performed in the first instance, as summarized in Table 1. With additional runs to cover follow-on investigations of parameter phase-space, over 40 simulations have been performed and analysed. An illustrative selection is presented in this paper, aiming to show as wide a range of behaviour as practicable. These are listed in Table 2.

In this Section, the four broad ranging constant inflow simulations are discussed. This is followed by a selection of pulse simulations, including rapid pulse simulations in both light and heavy jets, space-time diagrams of intermediate-pulse duration jets, and also slow pulsations in a selected jet configuration.

See the section DATA AVAILABILITY below to access data, including where the underlying 1000-frame movies of a selection of simulations are available in the Zenodo repository, at https://zenodo.org/records/11078517.

4.1 Jets with constant inflow speed

We need to distinguish between oscillations inherent to jets with constant inflow from those caused by the sinusoidal driven pulses. In fact, we will see that some constant inflow jets generate shock waves which propagate downstream as distinct pressure pulsations. These may mimic the propagation of imposed pulses, as well as being responsible for sweeping the ambient gas adjacent to the outer jet surface boundary out along the axial direction.

An example of the physical parameters of some of the four constant-inflow jets are illustrated in Fig. 1 (left panel), for a low overpressure low-density steady-state jet, and Fig. 8 (left panel) for a high overpressure heavy steady-state jet. These are cross-sectional snapshots at 200 time-units, i.e. the end of the simulations. The jets replicate some of the steady-state jets discussed by (Smith & Keogh 2022). Here, the jet tracer panels at the lower left have been improved to emphasize jet gas trapped in the ambient medium. This gas is maintained in the form of vortex rings, analogous to smoke rings.

We confirm that these non-pulsed jets do not transfer significant energy into the adjacent surroundings once the effects of the initial bow-wave has left the region. We have calculated the flux of energy through the cylindrical surface just within the displayed uniform region of length 27 $R_{\rm jet}$ and radius 13.5 $R_{\rm jet}$. We then find the average lateral power and axial power over the final 100 time-units (i.e. once the launched jet has settled down).

These lateral power out-flows are presented in Appendix A Table A1. This shows that the light non-pulsed jets transmit a very small percentage of the jet outflow power into the ambient medium once the jet head has advanced far beyond the near field of the nozzle. Less than 1 per cent net energy is transferred.

The heavy (high jet/ambient) density-ratio jets, on the other hand, have relatively large percentage power inflows from the ambient medium in towards the jet, reaching tens of percent. This may seem surprising until one recognizes the oscillations along the jet interface which drive the ambient gas adjacent to the jet outer boundary surface, advecting it in the axial direction. This sets up a large-scale

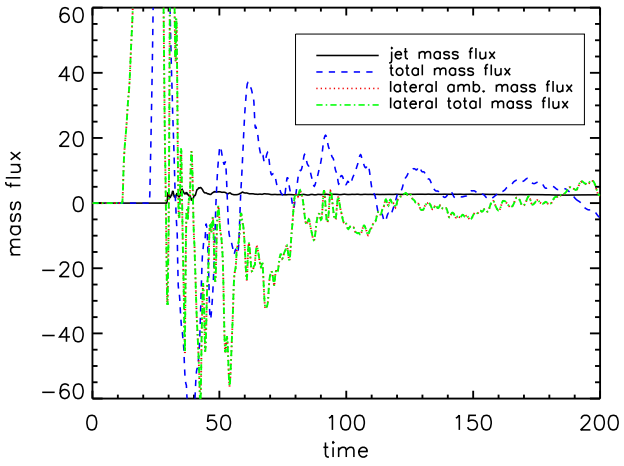

Figure 3. Rate at which mass flows across the cylindrical computational grid surrounding the jet axis. The initial bow shock reaches the tube surface at 13.5 $R_{\rm jet}$ at a time of 12 time-units and gas is swept out (dot–dashed line). After 20 time-units, the jet head reached the cylinder end-cap (dashed line). The launched jet (full line) then settles down to a roughly constant flow. However, the ambient medium displays large and variable mass transfer into the cylindrical computational grid through the outer-sleeve and out through the end-cap. The example shown here is the simulation designated as M2K2E0.1R10 which has $\kappa = 2$ and $\eta = 0.1$.

circulation, with surrounding ambient matter/energy drawn into the jet, replacing the advected medium.

As noted by Smith & Keogh (2022) from space-time diagrams and movies, the energy is transferred by the propagating surface waves which correspond to a form of Kelvin–Helmholtz instability. In the overpressured context, these waves lead to a pressure feedback loop via the ambient medium which causes the stand-off shock to oscillate in position and strength (see the Tam 1995; Franquet et al. 2015 reviews).

The circulation in the ambient medium caused by the jet oscillations is studied by examining the mass flux across the cylindrical surface over the second half of the simulation duration. The average mass fluxes are provided in the final column of Table A1.

In all cases, gas flows laterally into the jet and is swept axially out along with the jet. Fig. 3 displays the mass flow both axially and laterally for the low-density low-overpressure run which demonstrates relatively weak jet oscillations. Even in this case, the gas is efficiently circulated.

This shows that indeed a negative mass flux occurs laterally (green dot–dashed line), with the gas flowing in from the surrounding ambient gas reservoir. Consistent with this, a positive ambient mass flux (blue dashed line) accompanies the jet flow through the end-cap. If the jet flow were steady, we would not expect any advection once the jet channel is established. However, the jet walls invariably display oscillations caused by a feedback from pressure waves in the ambient medium and Kelvin–Helmholtz instabilities at the jet surface boundary. Hence, the ambient gas flow exhibits considerable variation.

Within the jet, the oscillatory motions do not generally appear as a coherent train of pulsations. One exceptional case is that of $\eta = 10$ and $\kappa = 2$ in which disturbances start at the stand-off shock and propagate downstream. The pulses are distinctly seen in the associated movie as well as in pressure space–time diagrams.

These naturally occurring pulses are inherent to a single jet and would not be expected to share the symmetry caused by central events which drive twin pulses within twin jets (e.g. Noriega-Crespo

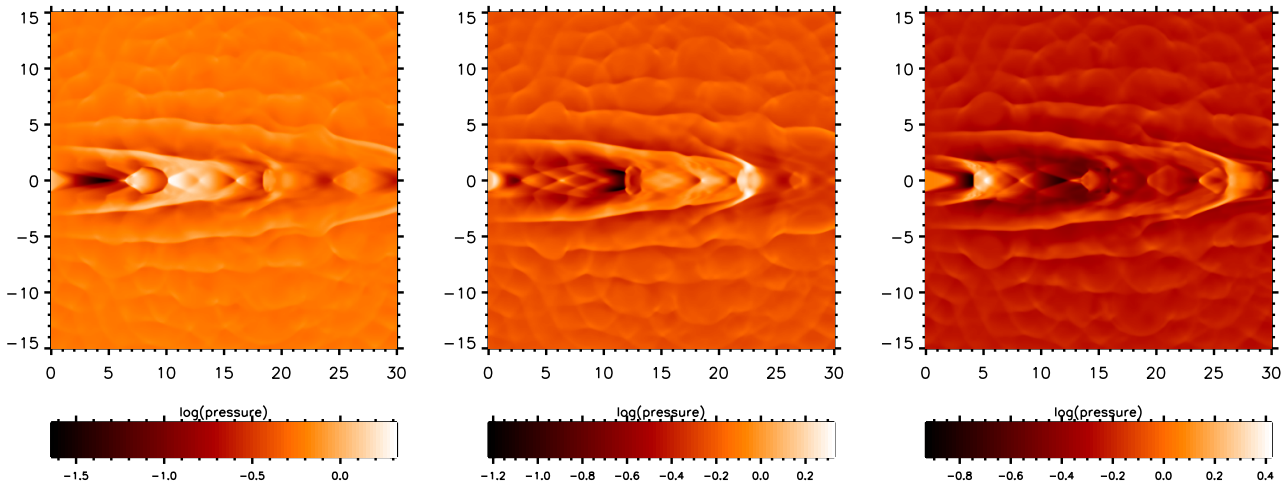

Figure 4. Time sequence for a rapid pulsating light low-overpressure jet. Pressure cross-sections over a brief time for the period 2 pulsed light Mach 2 jet with low overpressure, $\kappa = 2$, and low-density ratio, $\eta = 0.1$. The sequence runs from left to right at times 198.4, 199.0, and 199.6. The sinusoidal velocity pulses are of amplitude 40 per cent.

et al. 2020). On the other hand, there are many examples of twin-jets which do not contain symmetrically placed knots with various possible causes. For example, the HH 211 jets display stationary knots (designated BK1 and RK1, RK3) and outer knots that are difficult to pair up (Jhan & Lee 2016).

A selection of simulations are available in the Zenodo repository, at https://zenodo.org/records/11078517.

4.2 Rapid pulsations in light jets

We first analyse rapid pulsations in the light jet. We take a period of 2 and an amplitude of $\Delta v = 0.4 v_o$ in velocity. The diamond pattern associated with regular shock reflection is completely lost in this case. It is replaced by travelling sharp arc-shaped shocks which propagate down the jet at high speed. This motion is illustrated by the three pressure panels of Fig. 4, separated by 0.6 time-units.

Mach shock discs are present in individual arcs where fast jet material catches up with slower material. This is also evident on the axial velocity panel at the top right of Fig. 1. Occasionally, an oblique/conical shock pattern does return, as seen in the middle panel of Fig. 4. However, it is quickly eliminated by the passage of the next pulse.

A series of pressure ripples propagates in the ambient medium. This is caused by the short-time span of the jet pulses to reach the stand-off shock. This causes the entire interface to be vibrated at the rate of the pulsations.

The result is a remarkable pattern of ripples shown to propagate laterally out from the jet. These are cylindrical ripples which move out at a constant wave speed through the ambient medium. As with the ripples on the surface of a disturbed body of water such as a pond, the wavelength is maintained while the amplitude drops. The ripples are illustrated in the right panel of Fig. 5, which shows the pressure disturbances propagating radially away from the jet axis (solid line). For comparison, the non-pulsed equivalent is displayed in the left panel.

The precise nature of the ripples is elaborated by the cross-cut profiles at a location of 10 $R_{\rm jet}$ downstream of the nozzle in Fig. 5. This figure demonstrates a wavelength of the lateral ripples of $\sim 2.8 R_{\rm jet}$. With the period of 2, the wave speed is $1.4 c_{\rm amb}$. Hence the waves rapidly steepen into the classical sawtooth pattern as shown by the pressure and radial velocity profiles.

The wave motions will carry energy away and may be detectable as fronts. However, these are non-linear sound waves which build up into weak shock waves and so do not dominate the energy balance. Indeed, the radial speed is clearly inwards on average, towards the jet axis (red dot–dashed line) in Fig. 5.

At high overpressure a Mach shock disc is maintained in the constant velocity case, as shown in the left panels of Fig. 2. In this case, mild pressure waves are seen in the cross-sectional profiles of the left panel of Fig. 6. However, the Mach disc oscillates resulting in a quite turbulent jet downstream.

With pulsations added to the $\kappa = 8$ case, the location of the Mach shock varies violently, as evident from the disorganized strong pressure waves emanating into the ambient medium seen in the right panel of Fig. 6. Superimposing 40 per cent pulsations, much of the effect on the ambient medium remains (Fig. 2). However, the regular oscillations are no longer prominent and the Mach disc oscillates in position quite violently and can disappear, with a regular shock reflection present as shown in the middle panel of Fig. 7. Hence, unlike the low κ case above, the high overpressure controls the flow pattern with the pulsations providing large perturbations.

A selection of simulations are available in the Zenodo repository, at https://zenodo.org/records/11078517.

4.3 Rapid pulsations in heavy jets

The short-period simulations in which the jet is heavier than the ambient medium are fundamentally different. This is because the period is now shorter than both the dynamical time and surface wave time. Therefore, an entire pulse evolves within the divergent–convergent jet section before the stand-off shock is reached.

The result is that the inner cavity now acts as a bellows (right hand panels of Fig. 8), as shown by comparison with the non-pulsed jet equivalent (left panels). The inner cavity contracts and expands as the pulse propagates. We illustrate the results with the $\kappa = 8$ case, noting that the $\kappa = 2$ case is similar.

The pulse then interacts with the stand-off shock which stays roughly at the same position while pulses proceed downstream.

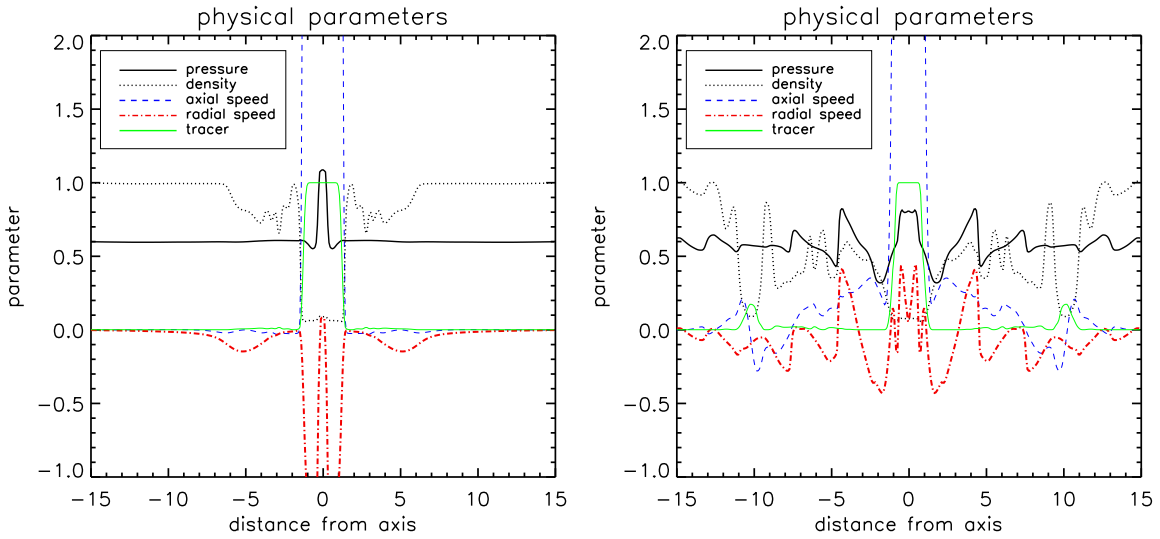

Figure 5. Lateral parameter profiles for light low-overpressure jets. Physical parameters are shown as a function of the radial distance from the jet axis, at an axial distance of 10 $R_{\rm jet}$ from the nozzle. The steady state jet (left panel) is compared to the rapid pulsation jet (right panel) for a light Mach 2 jet with overpressure ratio $\kappa = 2$ and density ratio $\eta = 0.1$. The sinusoidal velocity pulses are of amplitude 40 per cent and period 2, corresponding to the right panel of Fig. 4. Note that the jet axial and radial speeds are not displayed to their full magnitude.

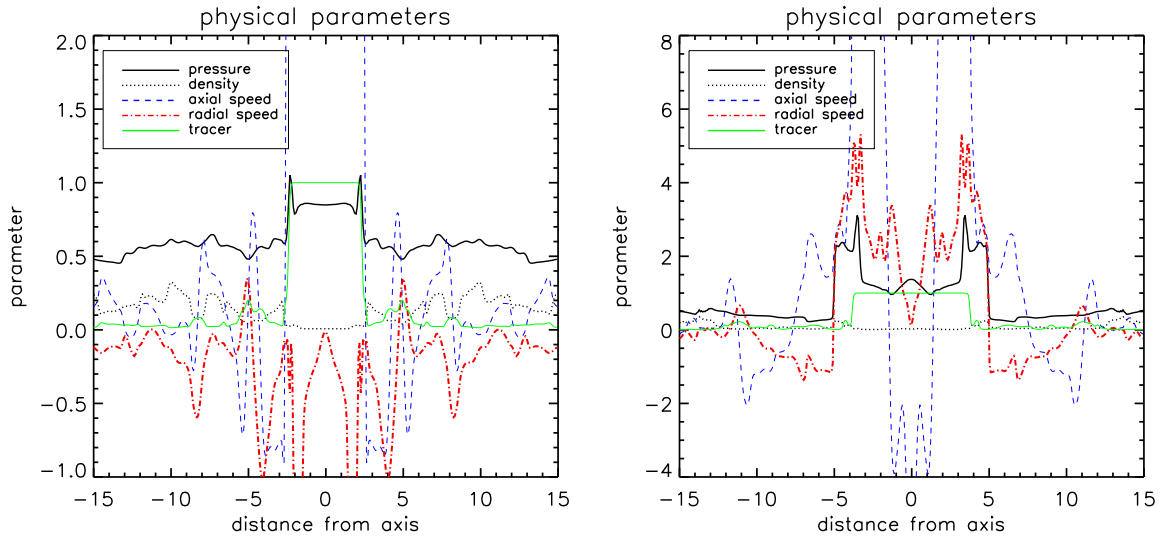

Figure 6. Lateral profiles for light high-overpressure jets. Physical parameters are shown as a function of the radial distance from the jet axis, at an axial distance of 10 $R_{\rm jet}$ from the nozzle. The steady state jet (left panel) is compared to the rapid pulsation jet (right panel) for a light Mach 2 jet with overpressure ratio $\kappa = 8$ and density ratio $\eta = 0.1$. The sinusoidal velocity pulses are of amplitude 40 per cent and period 2, corresponding to the right panel of Fig. 7. Note that the jet axial and radial speeds are not displayed to their full magnitude.

The density and velocity panels of Fig. 8 show that a thick tube of pulses is generated beyond the stand-off shock. Thus, the density and velocity panels display a remarkable pattern. The tube contains a series of moving thick annuli. In the pressure panel, however, it can be seen that the shock pattern is more complicated, with the jet tube not recognizable.

The region within the stand-off is subject to a series of impacts, generating the bellows. As seen in Fig. 9, a number of ripples are released into the ambient medium.

The stand-off shock changes shape. It often appears in an oblique shock configuration, with the shock cone apex facing the nozzle. Within the bellows, both advancing and receding shocks are present.

The ripples are shown graphically in Fig. 10. The falling amplitude as they propagate away from the axis is seen in the pressure and radial speed profiles.

A selection of simulations are available in the Zenodo repository, at https://zenodo.org/records/11078517.

4.4 Intermediate pulsations in light and heavy jets

For long-period pulses, the jet shock pattern can gradually adjust. We first consider intermediate duration pulsed jets. To analyse these, snapshots of the physical parameters do not capture the pulsation effects. Instead space–time diagrams are used to detail the pulses, although we are limited to displaying properties along the jet axis only. The space–time tool shows the jet evolutionary nature by

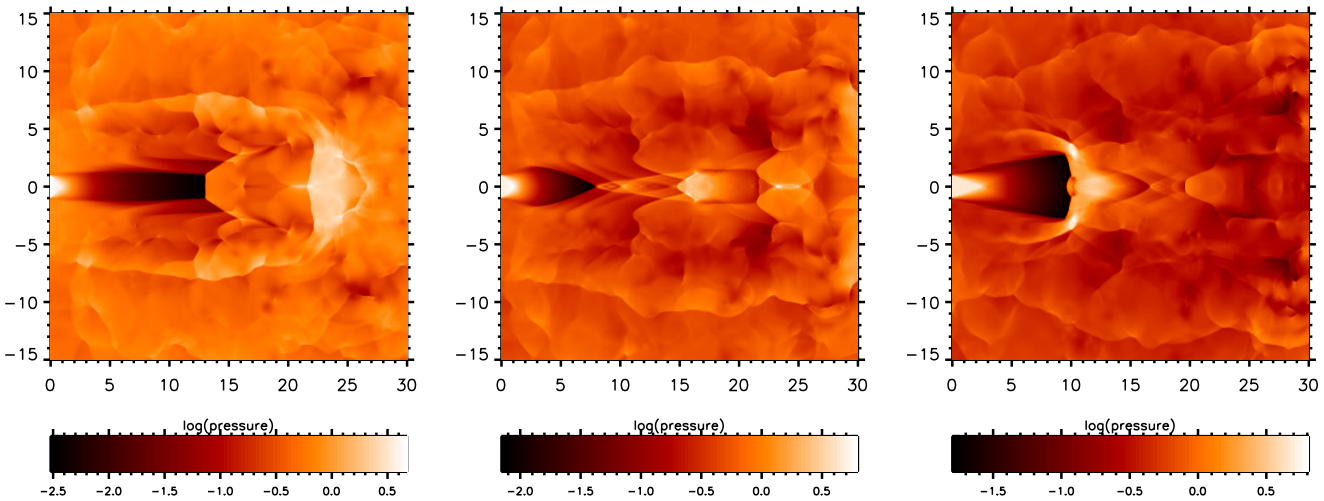

Figure 7. Rapid pulsation of light jet with high overpressure. Pressure cross-sections over a brief time for the period 2 pulsed Mach 2 jet with high overpressure ratio ($\kappa = 8$) and low-density ratio ($\eta = 0.1$). The sequence runs from left to right at times 198.4, 199.0, and 199.6. The sinusoidal velocity pulses are of amplitude 40 per cent.

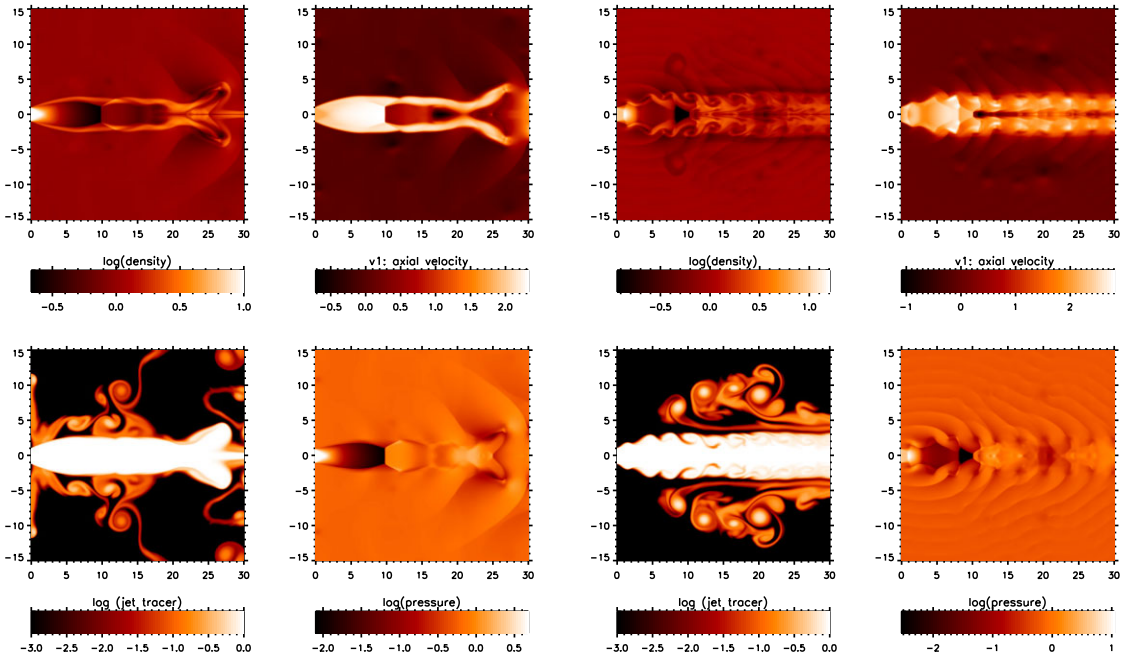

Figure 8. Effect of rapid pulsations on a heavy jet with high overpressure. A heavy ($\eta = 10$) Mach 2 jet with high overpressure ($\kappa = 8$) is considered, with comparison of the steady state jet (left panels) to the rapidly pulsed jet (right panels). Note the Mach disc shocks established on the left. The sinusoidal velocity pulses are of amplitude 40 per cent and period 2. These are cross-sectional snapshots at time 200.

displaying the pressure profile along the jet axis for each of the 1000 data-cashes, each separated by a time of 0.2 time-units.

Space–time diagrams for period $P = 10$ jets are displayed in Fig. 11.

The pulses dominate in both space–time evolutions, showing that forward and reverse travelling shocks overwhelm the steady recollimation patterns. Numerous secondary shocks temporarily appear before being swept into the main shocks.

The flow patterns show more intricate detail. The high speed of the light jet results in the production of well-separated bow shocks. As shown in Fig. 12 for an overpressure of 2, a newly created bow (left panel at time 186) propagated into the degenerating shock pattern established after the previous pulse. A short time later it has crossed the uniform grid (middle panel, time 188.2) with a bow speed of ~ 10, the average jet speed. There then follows an extended period in which stationary regular reflection shocks are established and slowly fade from the inside out as jet speed falls (right panel, time 192).

This contrasts with the high overpressure case with high-jet density shown in Fig. 13. The Mach shock drives out an associated bow wave and then collapses back before being overtaken by the next pulse. The flow is quite turbulent and no stationary shock pattern occurs at any time.

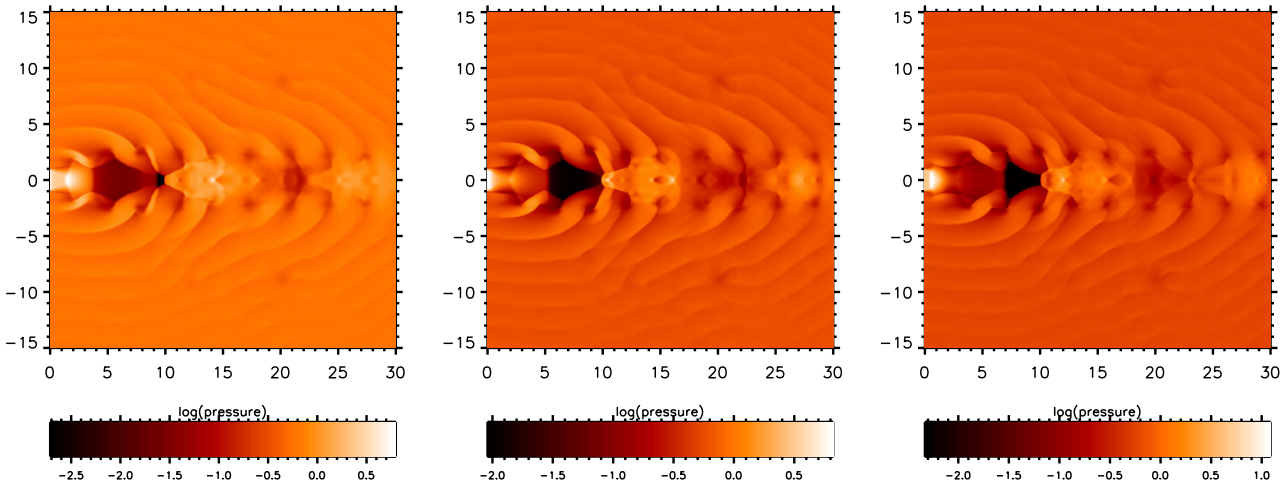

Figure 9. Rapid pulsation of a heavy jet with high overpressure. Pressure cross-sections over a brief time for the period 2 pulsed Mach 2 jet with high overpressure ($\kappa = 8$) and high-density ratio ($\eta = 10$). The time sequence runs from time 198.4, 199.0, and 199.6 The sinusoidal velocity pulses are of amplitude 40 per cent.

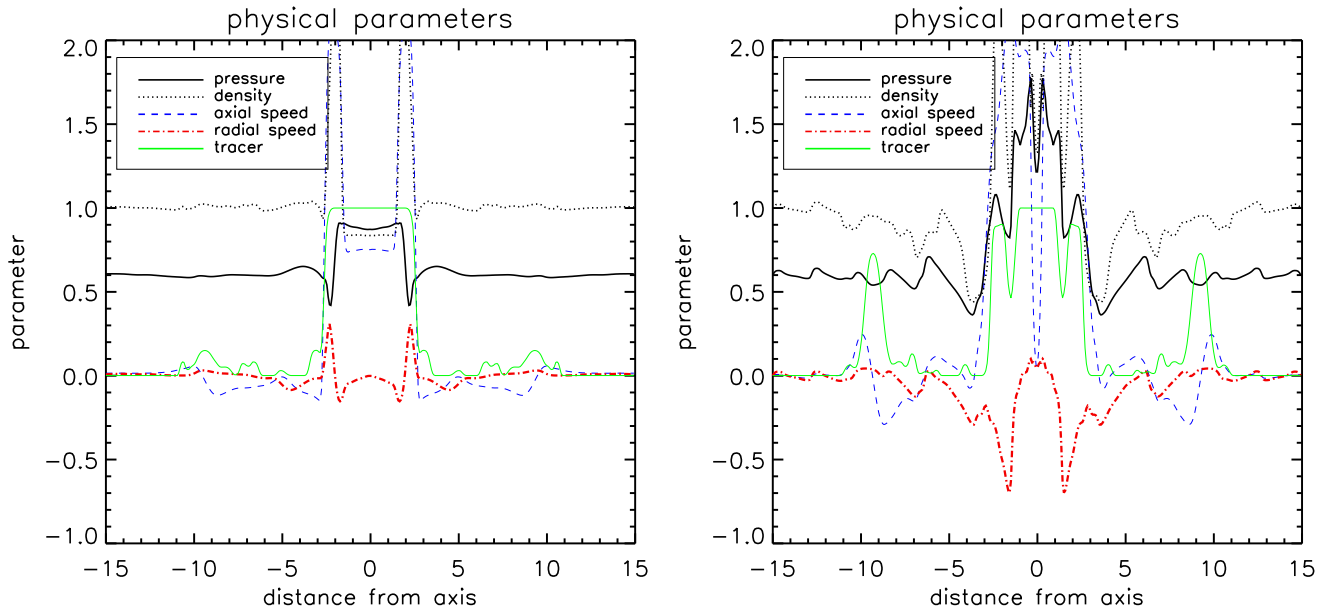

Figure 10. Lateral profiles for heavy high-overpressure jets. Physical parameters are shown as a function of the radial distance from the jet axis, at an axial distance of 10 $R_{\rm jet}$ from the nozzle. The steady state jet (left panel) is compared to the rapid pulsation jet (right panel) for a heavy Mach 2 jet with high overpressure $\kappa = 8$ and high-density ratio $\eta = 10$. The sinusoidal velocity pulses are of amplitude 40 per cent and period 2, corresponding to the right panel of Fig. 8. Note that the jet axial speed is not displayed to its full magnitude.

For the heavy jet, the train of bows can be seen on a single near-field image, as shown in Fig. 13. The dynamical time to cross the grid is $\sim$ 15 time-units, longer than the pulse period of 10.

To summarize, each pulse creates a distinct bow shock which penetrates the ambient medium. According to density and over-pressure, a variety of bow waves and internal shock structures are generated. Here, we note that the high-density jets produce a trail of smooth wide pressure-bows while the low-density jets produce well-spaced narrow pressure-bows. This is due to the large difference in dynamical times with a fixed pulse period.

Hence, these intermediate pulsed jets may correspond to restarting jets (Shulevski et al. 2015; Shabala et al. 2020). A much longer time between pulses would be needed to produce double–double and relic radio galaxies (Schoenmakers et al. 2000; Walg et al. 2014).

A selection of simulations are available in the Zenodo repository, at https://zenodo.org/records/11078517.

4.5 Slow pulsations in light jets

We illustrate long duration pulses by taking a period of 40.

We expect the flow pattern to transform across quasi-stationary flow patterns corresponding to the varying input Mach number. In order to broaden the jet-parameters selected, a light jet is

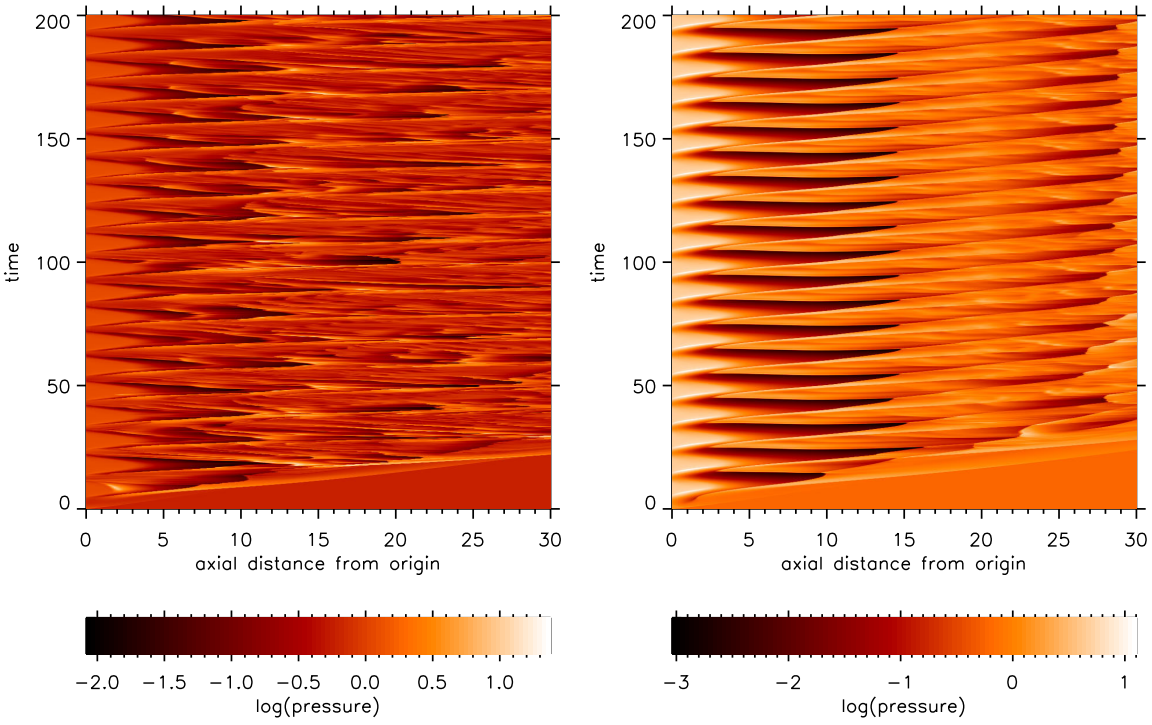

Figure 11. Space–time diagrams for intermediate-period pulsed jets. The left panel shows a low overpressure and low-density jet (M2K2E0.1R10P10V2.0). The right panel shows a high overpressure and high-density jet (M2K8E10R10P10V2.0). Both jets are subject to pulses with an intermediate-period of 10 time-units and amplitude of 100 per cent.

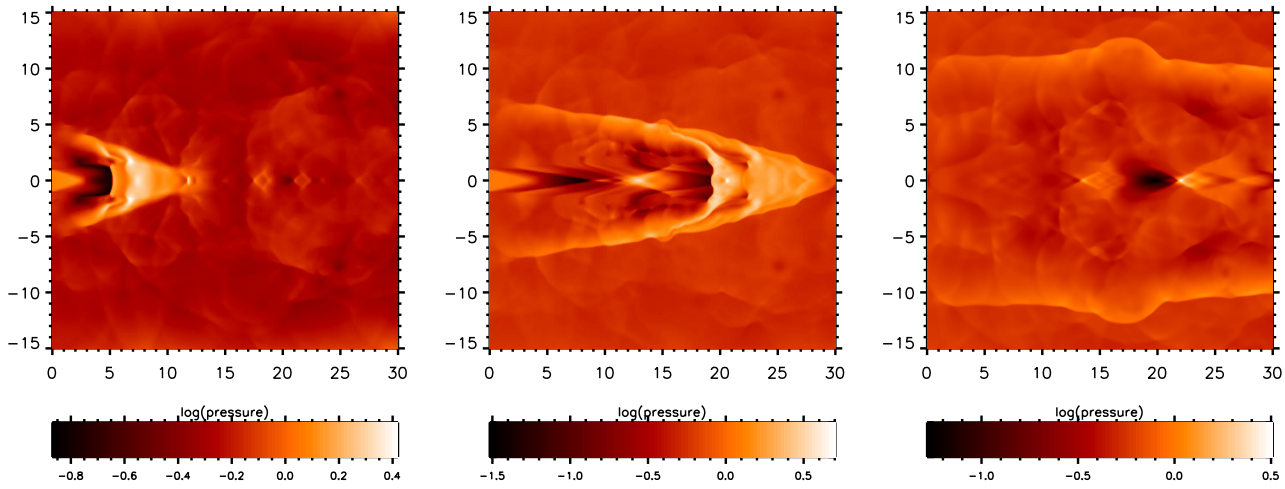

Figure 12. Intermediate period pulsation in a light jet with low overpressure. Pressure cross-sections for the period 10 pulsed light Mach 2 jet with low overpressure, $\kappa = 2$, and low-density ratio, $\eta = 0.1$. The sequence runs from left to right at times 186.0, 188.2, and 192.0. The sinusoidal velocity pulses are of amplitude 100 per cent.

illustrated with an intermediate pressure/ratio of $\kappa = 3.5$, designated M2K3.5E0.1R10P40V1.4.

Fig. 14 compares parameters between the constant inflow jet (left panels) and the long-duration pulsed jet (right panels), at the end of the simulation. Both density and jet-tracer panels show more extensive turbulence surrounding the pulsed jet.

The overpressure of 3.5 is the critical value which separates regular reflection from Mach shock discs, at Mach 2. Hence, a long-period time sequence displays both times when each of these shock patterns are well established. This is illustrated in Fig. 15, which along with the lower-right subpanel of Fig. 14, covers the major phases of a 40 time-unit period jet.

The contrasting internal motions within jets are revealed through space–time diagrams. Fig. 16 shows that the structural changes are dominated by the primary pulsation period with fast oscillations superimposed for the $P = 10$ and $P = 40$ runs. However, there are discernible long-term variations even for the $P = 2$ simulation (left panel) of order ~ 30 time-units. These are related to the large-scale turbulent motions which remain in the slow-moving ambient gas.

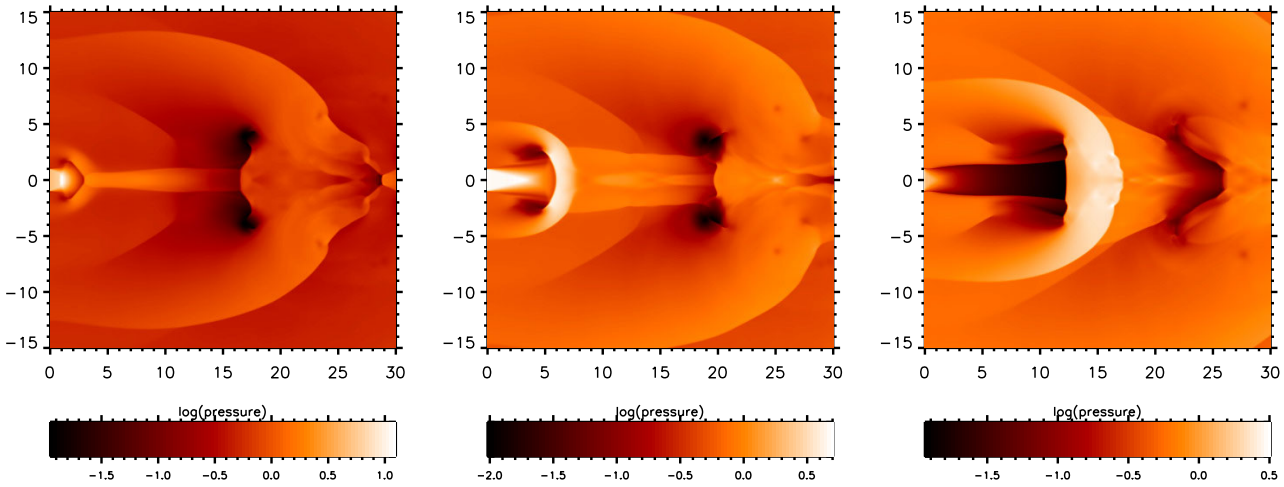

Figure 13. Intermediate period pulsation in a heavy jet with high overpressure. Pressure cross-sections for the period 10 pulsed heavy Mach 2 jet with high overpressure, $\kappa = 8$, and high-density ratio, $\eta = 10$. The sequence runs from left to right at times 186.0, 188.2, and 192.0. The sinusoidal velocity pulses are of amplitude 100 per cent.

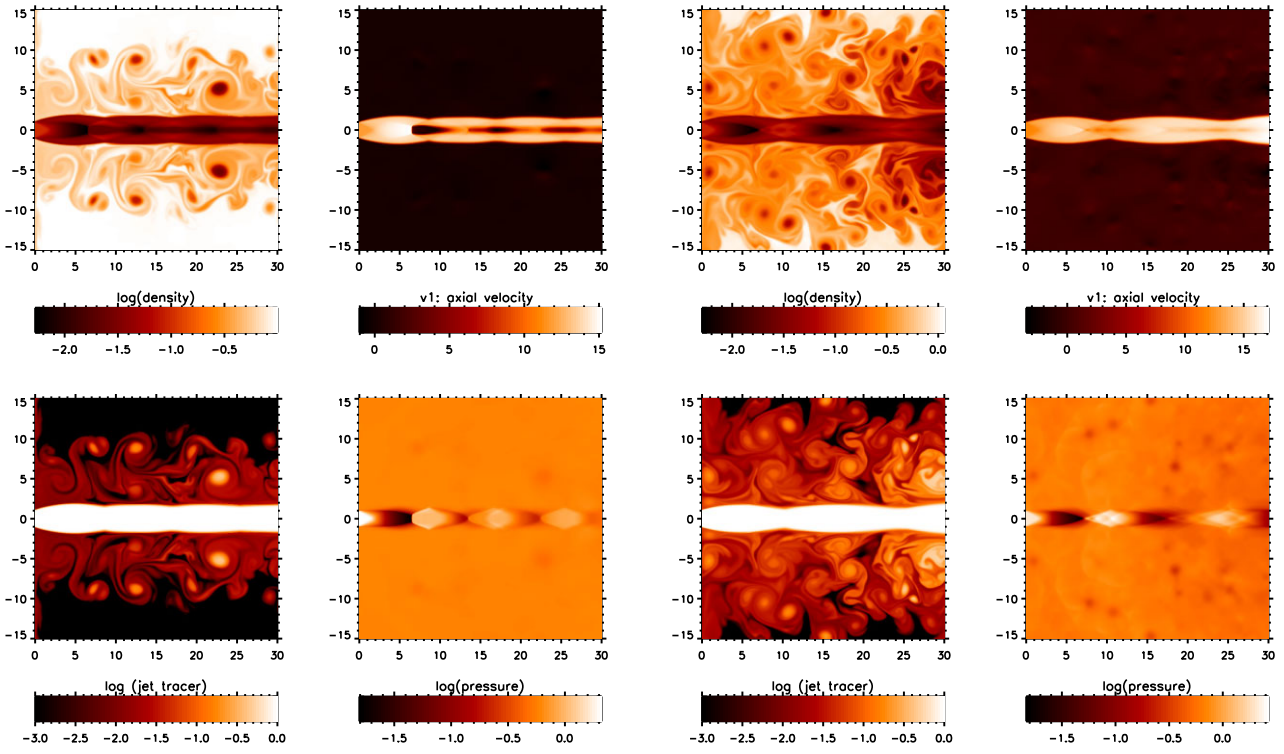

Figure 14. Effect of slow pulsations on a light jet with an intermediate overpressure. A light ($\eta = 0.1$) Mach 2 jet with an intermediate overpressure ($\kappa = 3.5$) is considered, with comparison of the steady state jet (left panels) to the slow pulsation jet (right panels). The sinusoidal velocity pulses are of amplitude 100 per cent and period 40. These are cross-sectional snapshots at time 200.

A selection of simulations are available in the Zenodo repository, at https://zenodo.org/records/11078517.

5 ENERGY DISTRIBUTION AND MASS TRANSFER

In this Section the question of jet support of the ambient gas in the environment against gravitational collapse is examined. Specifically, we consider what type of pulsating jet would transmit and heat the ambient medium beyond the uniform part of the cylindrical regime. We calculate the flow of energy through both the computational end-cap and sleeve surfaces of a virtual cylinder located at 90 per cent of the uniform grid region.

We know that the initial advancing bow is ~ 70 per cent efficient at transferring energy, into mainly heating the ambient gas, however we are interested here in the long-term support of the medium in the near-field of the nozzle. Therefore, we have calculated the energy

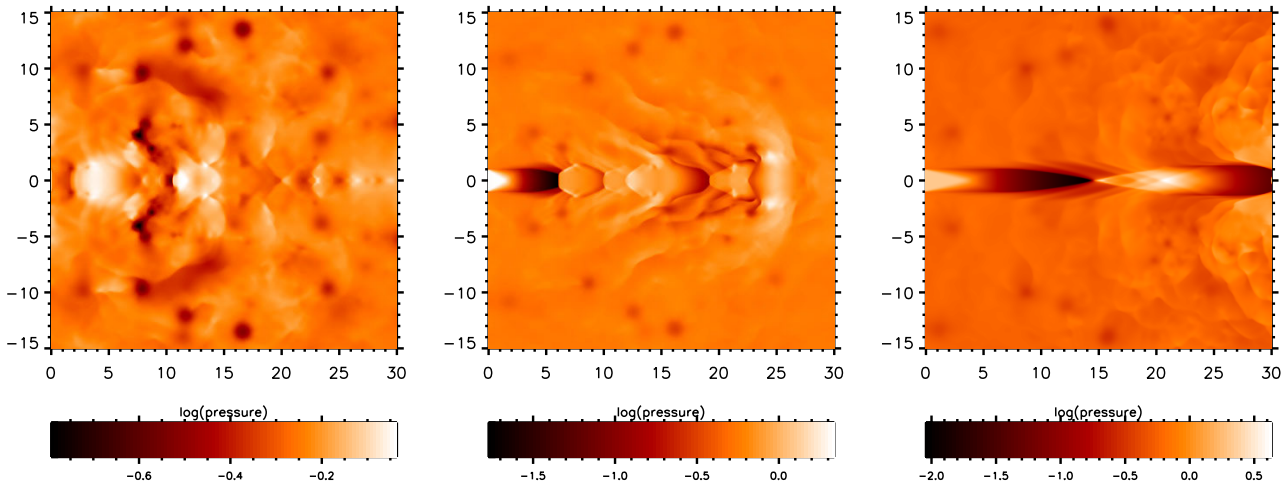

Figure 15. Long-period pulsation in a light jet with intermediate overpressure. Pressure cross-sections for the slow pulsed Mach 2 jet with intermediate overpressure, $\kappa = 3.5$, and low-density ratio, $\eta = 0.1$. The time sequence runs from left to right at times 170.0, 180.0, and 190.0 The sinusoidal velocity pulses are of amplitude 100 per cent and period 40.

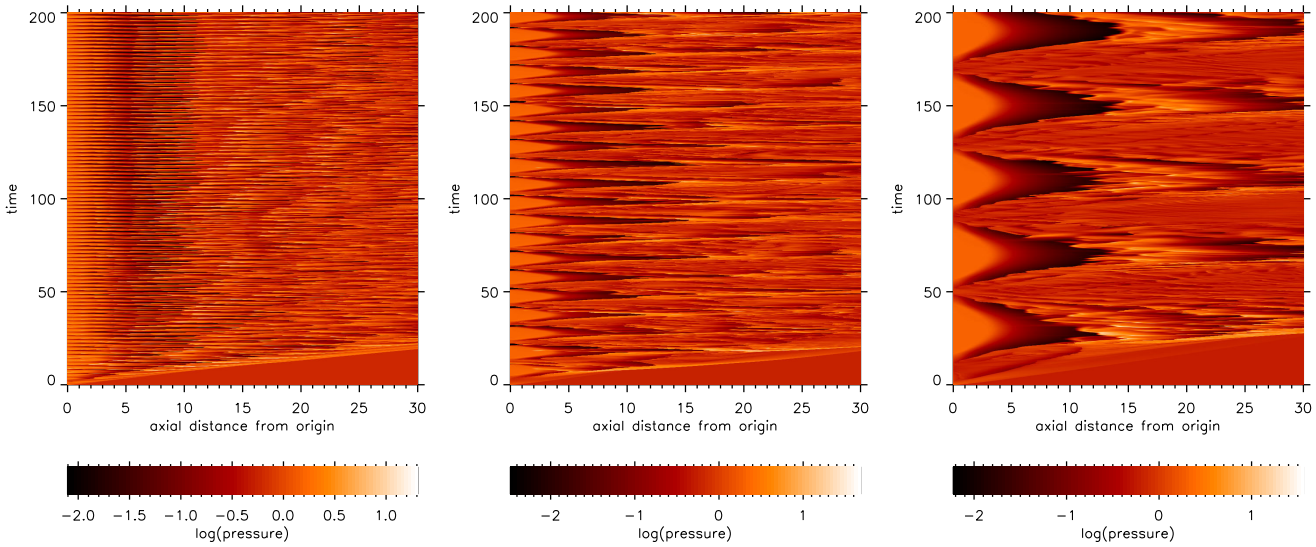

Figure 16. Pressure variations along jet axes as a function of time. Space–time diagrams for $\kappa = 3.5$ jets with fast ($P = 2$), intermediate ($P = 10$), and slow ($P = 40$) pulsations from left to right. For Mach number $M = 2$, we fix $\eta = 0.1$, and a pulse amplitude of 100 per cent.

distributions in the final half of the simulations, between times of 100 and 200 time-units, when jet initiation effects have subsided.

The major findings are that the net flow of energy into the ambient medium can be radially inwards as often as outwards. Thus, energy can be taken from the ambient medium adjacent to the jet surface boundary and extracted through the end-cap, setting up an advection pattern.

A clear example is shown in the upper panel of Fig. 17 for a low κ, where the negative values for lateral power (red dotted line) indicate inflow. Note that the lateral power has an initial peak at early times in all the diagrams: the advancing bow reaches the computational grid cylinder sleeve census surface well before the jet reaches the computational end-cap. It should also be noted that the motions are subsonic and the lateral energy is in the form of thermal rather than kinetic (green dot–dashed).

A high-overpressured jet yields a net lateral inflow of energy at high-pulse rates. An example is shown in the middle panel of Fig. 17 where there is a large exchange in both directions, however the net flow is negative. While on the other hand, there is strong lateral energy outflow for the intermediate period pulses displayed in the lower panel.

Of the initial pulse simulations carried out (16 out of 24), there was an overall power inflow toward the jets (see Appendix A, Table A2). However, the high-overpressure, low-density ratio jets had significant energy outflows. As a result, further simulations were then carried out for intermediate values of jet/ambient pressure ratios. Low-density jet/ambient ratio simulations were repeated for overpressures of 3.5 (the threshold above which Mach discs dominate), 4, and 6 (see Appendix A, Table A3), and for maximum velocity amplitudes. Of these additional nine simulations, six had significant lateral power out-flows, including the highest peak lateral power out-flow discovered.

The average lateral powers are plotted against pulse period in Fig. 18, both in linear and logarithmic forms. For an overpressure

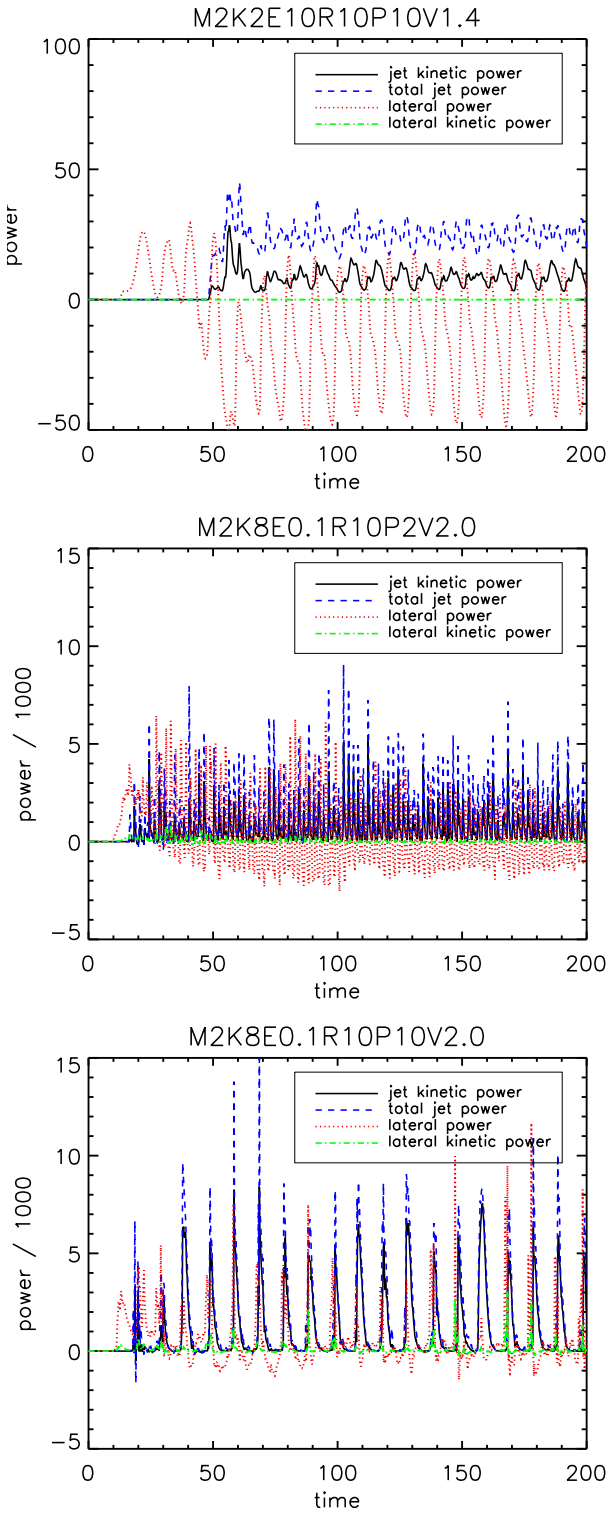

Figure 17. Power versus time for pulsed overpressure jets. We present examples where the lateral energy flux across the cylindrical boundary is predominantly negative (upper panel), net negative (middle panel), and predominately positive (lower panel). Normalized power units are in terms of the jet radius, ambient density, and sound speed ($\rho_{\rm amb}c_{\rm amb}^3 R_{\rm amb}^2$). The simulations are as designated and tabulated.

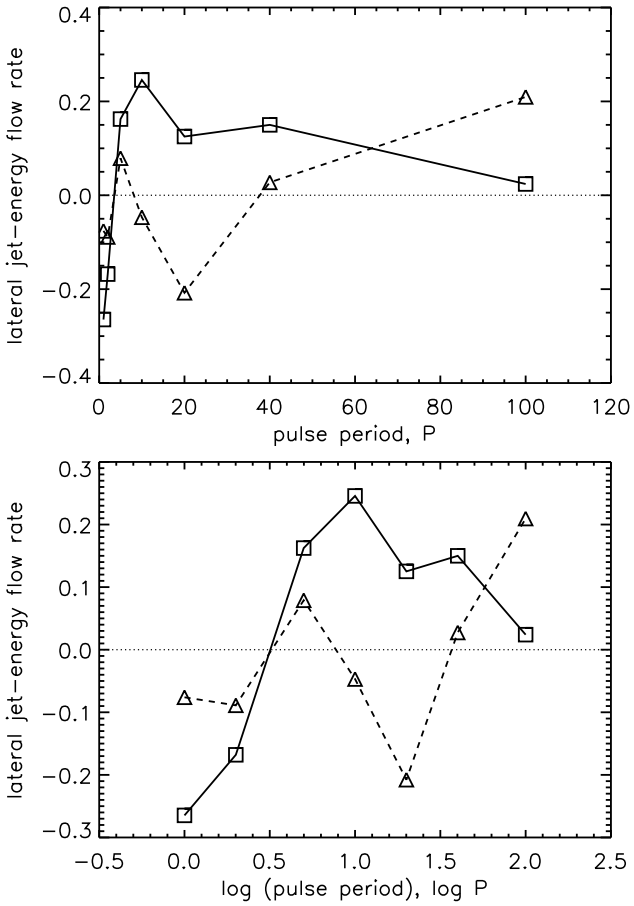

Figure 18. Power transmitted to the ambient medium versus pulse period. The mean lateral energy flow rate calculated across a computational cylindrical sheath located at a radius of $13.5R_{\rm jet}$ from the jet axis, over the final half of the 200 time-unit simulations. Overpressures of $\kappa = 8$ (connected by solid line), $\kappa = 2$ (connected by dashed line), are considered for low-density ratio $\eta = 0.1$ jets and for 100 per cent pulse amplitude. Normalized data is presented linearly (upper panel) and with logarithmic period (lower panel).

of 2, the power flow represented by the triangle symbols, is mostly laterally inwards for the short- and intermediate-pulse periods. Only for the longest periods, however, is the net energy flow consistently outwards.

We note that low-overpressure jets generate a quasi-steady diamond shock pattern. The outer pulses may advect some material close to the interface where jet-ambient mixing occurs. The gas removed through the end-cap is replaced by inflow through the cylinder sleeve.

For higher overpressure jets, there exists an intermediate range of pulse periods for which strong positive energy outflows are recorded (square symbols in Fig. 18.) This does not hold for high-density jets, as can be seen in Table A2. Interestingly, this regime was found to be associated with the propagation of a train of bow shocks. Hence, to maximize energy dispersal from the jet requires moderate pulse periods, of order of the Kelvin–Helmholtz time-scale.

To further investigate this, we have run simulations at a number of overpressures. As shown in Fig. 19, pulses with intermediate pulse periods within the high-overpressured regime can transmit significant jet energy into the adjacent ambient medium. For $\kappa \geq 4$, over 20 per cent of the jet energy can be transmitted laterally. The simulation with a peak in the lateral power out-flow was obtained for an intermediate pulse period of 10 time-units, and for an intermediate

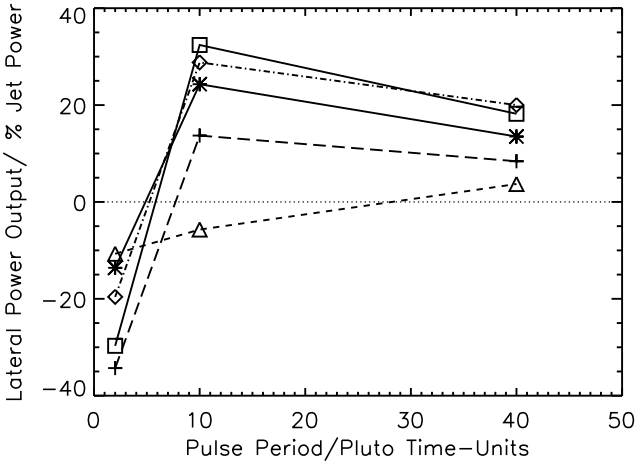

Figure 19. Percentage lateral power versus pulse period for various overpressures. M2E0.1 R10V2.0 jets with various pulse periods P and overpressures K: $K2 = \triangle$, $K3.5 = +$, $K4 = *$, $K6 = \square$, $K8 = \diamond$. From the graph it is clear that there is a maximum in percentage lateral power outflow for intermediate pulse durations, and for an intermediate overpressure.

jet/ambient pressure-ratio of 6. This configuration had an associated lateral power out-flow of 32 per cent (see Appendix A, Table A3).

In summary, there is a maximum in lateral power out-flow at an intermediate pulse duration and intermediate overpressure. Note that higher-overpressure jets have stand-off shocks which are Mach discs, whereas the low-overpressure jets, with $\kappa = 2$, have an oblique/weak stand-off shock. By interpolation, it appears that significant lateral power out-flows occur for pulse duration greater than about five time-units i.e. greater than the Kelvin–Helmholtz surface wave crossing time to the stand-off shock. This is a maximum of 4.72 time-units for $\kappa = 8$ (see Section 4.2). There is a peak in percentage power for the higher overpressure jets which occurs at slightly different pulse durations depending upon the overpressure, but appears to be at an average of about 14 time-units. This compares to about three times the jet Kelvin–Helmholtz surface wave crossing time.

Lateral Inflows of energy are enhanced for short-duration pulses (see Fig. 19). The rapid pulses enhance engagement between the jet boundary and the adjacent ambient gas, compared to steady-state jet configurations. Note that the short-period pulse duration of 2 time-units compares to about four times the corresponding steady-state jet-dynamical time, and about half the jet Kelvin–Helmholtz surface wave crossing time. An additional simulation was carried out for the highest overpressure jet and for a pulse duration of 1 time-unit, where the percentage lateral power in-flow was further enhanced from 20 per cent to 30 per cent of jet power.

The long pulse duration jets temporarily transition to a pseudo-steady-state high Mach jet, where for such steady-state jets there is generally an overall power out-flow, although small in magnitude (Smith & Richards 2023). The pulse period of 40 time-units is an order of magnitude greater than the Kelvin–Helmholtz jet surface wave crossing times. From Fig. 19, the percentage lateral power out-flows appear to decrease with increasing pulse duration. An additional simulation was carried out for the highest overpressure jet and for a pulse duration of 100 time-units, where the percentage lateral power had continued to fall to near zero.

The redistribution of ambient mass is significant in all the jet simulations. The results are summarized in Fig. 20. Mass is advected from the ambient medium and swept through the end-cap for high-frequency pulsations. This also generally holds for low overpressures

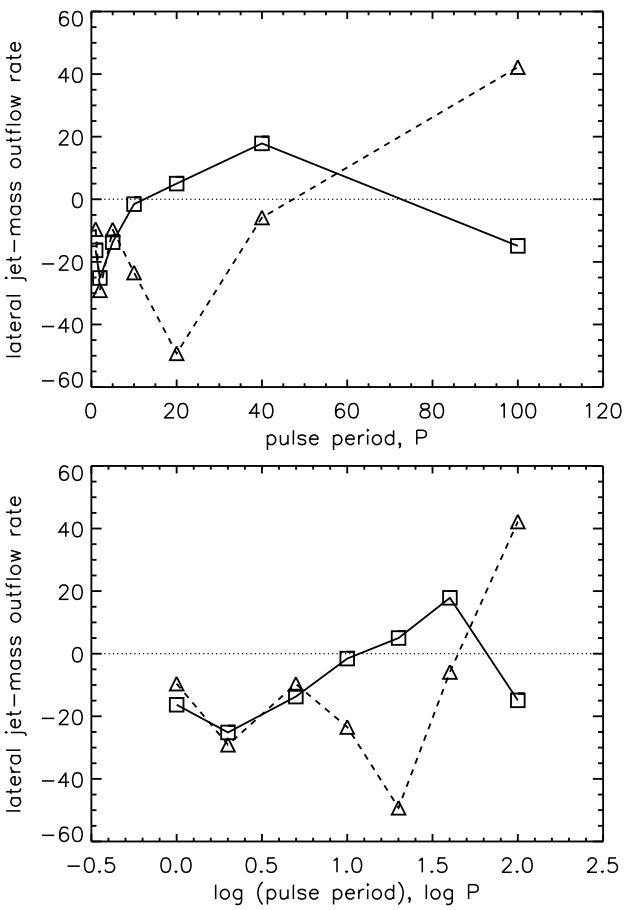

Figure 20. Net rate of mass flowing laterally for various jet configurations. The mean mass flow calculated across a computational cylindrical sheath located at a radius of $13.5R_{\rm jet}$ from the jet axis during the final half of the 200 time-unit simulations. Overpressures of $\kappa = 8$ (connected by solid line), $\kappa = 2$ (connected dashed line), are considered for low-density ratio jets ($\eta = 0.1$), and for 100 per cent pulse amplitude. Normalized data is presented linearly (upper panel) and with logarithmic period (lower panel).

as illustrated in the top panel of Fig. 21. For high overpressures however, mass can be expelled laterally for lower frequency oscillations, as shown in the lower panel of Fig. 21.

6 DISCUSSION

The combination of pulses and overpressure generates novel flow patterns. In particular, the classical diverging–converging jet undergoes bellows-like expansion and contraction. This sends pressure waves into the ambient medium which form steepening evenly spaced ripples when the pulsations are sinusoidal.

This mechanism could contribute to how the active galactic nuclei (AGN) jets are capable of making a significant contribution to moderating galaxy cool-gas in-flows, and help to explain observed limited galaxy star-formation rates. Steady flow Mach 2 jets have previously been studied, which indicated that significant lateral power output is not achieved (Smith & Keogh 2022). Here, we have built upon this work by allowing large velocity pulses travelling along the jet.

Alternative means of transmission of energy have been proposed in the literature. For example, it is considered that when jet-driven bubbles are disrupted by hydrodynamic instabilities, relativistic bubble

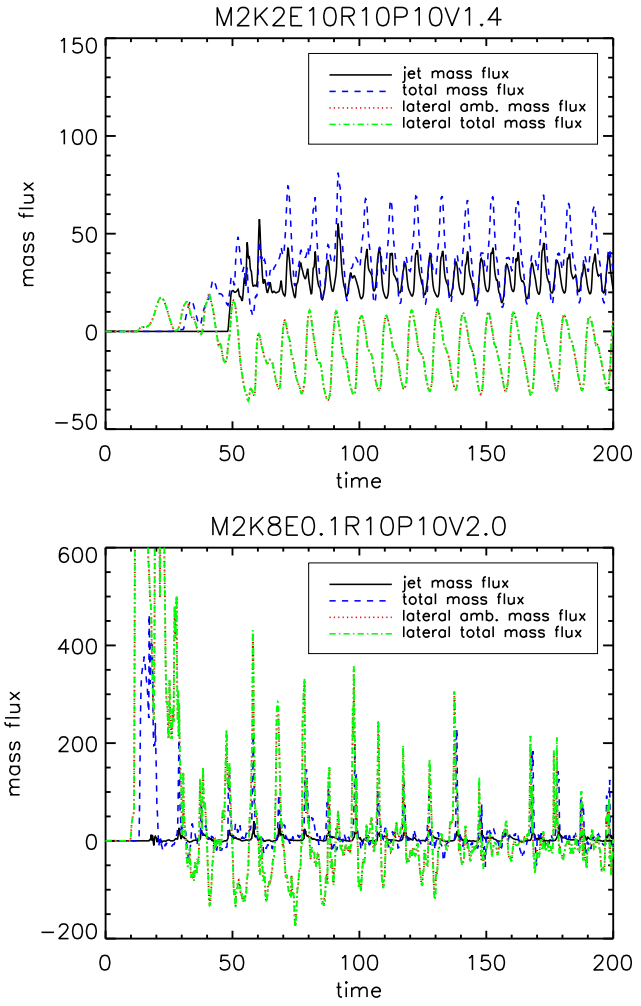

Figure 21. Mass redistribution versus time for moderately pulsed low- and high-overpressure jets. We take intermediate periods $P = 10$, for a low overpressure, $\kappa = 2$, high-density ratio, $\eta = 10$, jet and a high overpressure, $\kappa = 8$, low-density ratio, $\eta = 0.1$, jet. Normalized units are in terms of the jet radius, ambient density, and sound speed. Graph titles are the simulation designations.

plasma is mixed with the ambient medium, which could lead to gentle heating by mixing (Hillel & Soker 2017). Heat could be distributed by turbulent motions driven by bubble shredding or through large-scale convective motions (Yang & Reynolds 2016). In the shredding process, cosmic rays accelerated in the jets/bubbles may be released that could carry significant energy and diffuse rapidly throughout clusters (Guo, Oh & Ruszkowski 2008; Pfrommer 2013; Yang & Reynolds 2016; Ruszkowski, Yang & Reynolds 2017; Ehlert et al. 2018). Alternatively, thermal conduction has been invoked to transfer heat from the bubble wakes into the cluster cooling flow (Chen, Heinz & Enßlin 2019).

Whatever contribution AGN jets may make to moderating galaxy cool-gas in-flows, and despite the need for additional jet physics and further work, we have established that pulsed jet configurations exist with lateral power outputs being a large fraction of jet power (up to about 30 per cent). These have the potential to moderate galaxy cool-gas in-flows, where e.g. Su et al. (2023) estimates the power required to adequately moderate cool-gas in-flows to be of the order of 10^{43} ergs s^{-1}. AGN jet powers vary widely, with estimates of higher energy jets in the literature of order 10^{45} ergs s^{-1}. Such powers are consistent with the jets described here as shown by Su et al. (2023).

In Appendix B, we quantify the present model by comparing the energy needed to suppress cooling in the CGM to that which can be supplied by an overpressured jet. This does involve several big back-of-the-envelope assumptions, but does indicate that jets have the potential to heat the CGM within CGM cooling times.

A key objective is also to progress understanding of jet dynamics and attribute observed AGN jet luminosity distributions to their underlying physical parameters through observational diagnostics. Data of sufficient resolution and dynamic range are sparse at present but will be forthcoming soon through the Square Kilometre Array for AGN jets and the Extremely Large Telescope for protostellar jets (Peeples et al. 2019). It is hoped that the findings here may help lead to better parameter constraints. For example, recent reported observations of the AGN jet from 3C 78 (Roychowdhury et al. 2023) show that bright sources of luminosity along the jet, believed to be shock fronts, are seen to oscillate widely away from and towards the host galaxy over long periods of time. Roychowdhury et al. (2023) also refers to observations of accelerating and decelerating knots in e.g. the visible jet of M87. These observations may be associated with a Mach disc undergoing large oscillations similar to the shock front bellows characteristics we have found. Also, the ripples uncovered here may well be related to those detected in the cores of the Perseus cluster (Fabian et al. 2003; Sanders & Fabian 2007) and the Centaurus cluster (Sanders & Fabian 2008).

The channels cut by non-pulsed jets are not generally fixed but display continuing high-frequency oscillations referred to as screeching and noise (Powell 1953; Smith & Keogh 2022). The oscillations are maintained by a feedback loop as described by Wong et al. (2023). The ambient medium adjacent to the jet surface boundary is driven along by the jet, which results in an overall convective back-fill/in-flow of ambient energy and mass. The variation in local jet conditions, and axial oscillation of the shock front would also result in a cyclic variation in jet radius and therefore enhance the engagement of the travelling jet with the adjacent ambient medium. This mechanism is considerably enhanced for pulse simulations (see Table A2), particularly for rapidly pulsed jets.

The ambient pressure is subject to variation due to the jet impulses. However, the large ambient reservoir assures that in the long run, the average pressure adjacent to the jet is restored. A cocoon of lower density but higher temperature often persists which influences the surface waves and feedback.

The jets with long-period pulses cycle between low and higher Mach pseudo-steady-state jet configurations, where although energy out-flow mechanisms generally dominate, they are low in magnitude (Smith & Richards 2023). It was found that the small-amplitude shock front oscillations found in many steady-state jets (Smith & Keogh 2022) were preserved when jets were subjected to energy pulses. The shock front oscillations were more pronounced in the light, low-density-ratio jets, which are higher power jets, compared with the heavy, high-density-ratio, lower power jets.

A main finding is that the net flow of energy is radially inwards in the majority of cases studied. Mass/energy is taken from the ambient medium adjacent to the jet surface boundary and driven along with the jet, setting up an advection pattern. However, for higher overpressure and low-density-ratio jets, there exists an an intermediate range of pulse periods for which strong positive energy outflows are established. Interestingly, this regime was found to be associated with the propagation of a train of bow shocks.

The redistribution of ambient mass is significant in all the jets. Mass is advected from the ambient medium and swept along with the jet flow for high-frequency pulsations. This generally holds for low-overpressure jets. For high overpressures however, mass can be expelled laterally for intermediate frequency oscillations. In this paper we note that lateral mass outflows may contribute to observed CGM metallicity, but we do not attempt to quantify.

We found that there is a peak in percentage lateral power for the higher overpressure jets which occurs at slightly different pulse durations depending upon the overpressure, but is an average of about 14 time-units. This compares to about three times the jet Kelvin–Helmholtz surface wave crossing time. The physics behind the peak in lateral power for an intermediate pulse period will be investigated utilizing additional simulations as part of further work.

For the higher pressure-ratio intermediate-pulse duration jets, the large oscillations in the stand-off Mach disc appear to act as a bellows. Repeatedly, a slower section of jet, from a low velocity part of the pulse cycle, is caught up by a following faster section of jet, from the higher velocity part of the pulse cycle. This results in compression of the ambient near the jet-boundary surface, generating significant lateral pressure waves, and transferring a significant fraction of jet power. Note that this only leads to significant lateral power out-flows if the pulse duration is associated with moderate pulse periods, greater than, but comparable to, the Kelvin–Helmholtz surface wave crossing time to the stand-off Mach shock disc. The period of these energy pulses is the same as the velocity pulses of the jet, and are in-phase with the velocity pulses.

7 CONCLUSIONS

We have performed and analysed two-dimensional axisymmetric simulations of hydrodynamic jets. In particular, we obtain an initial understanding of the fundamental physics of the effect of velocity pulses travelling along overpressured jets.

We carried out a systematic survey for a wide range of pulse parameters within an initially constant density ambient medium. We varied pulse frequency and amplitude, while fixing a low Mach number of 2 for the jet. Parameters were chosen bearing in mind the internal dynamical speed, and the surface Kelvin–Helmholtz wave speed, based on the time to reach the first/stand-off shock. This splits the pulse types into fast, intermediate, and slow.

This is in the context of exploring shock structures within the near-field of an exiting high-pressure jet. Ultimately, we wish to determine if pulsed jet configurations exist with sufficiently large lateral energy outflows to drive moderation of galaxy cool-gas in-flows. However, this study may also help to interpret supersonic gas jets more generally.

A general mechanism was identified in Smith & Keogh (2022) for low Mach steady-state jets, where the ambient adjacent to the jet boundary is driven along with the jet. We found that ambient gas is advected out along the jet direction by rapidly pulsed jets. The pulsations vibrate the interface and so transfer momentum. The result is that mass and energy are convected in toward the jet to replace this gas, leading to a reduction of gas from the ambient reservoir.

The extraction of ambient gas in this manner may promote the recycling of material in galactic environments. If this gas has been polluted through star formation activity, then the outflow go on to pollute gas external to the galaxy. This may contribute to the high metallicities in cluster gas (Gatuzz et al. 2023a, b). Jet-driven bubbles have already been invoked in order to interpret hot metal-rich outflows aligned with X-ray cavities (Duan & Guo 2018).

At the other extreme, long-duration pulsed jets temporarily transform to pseudo steady-state jets, with very low-lateral power out-flows of mass or energy.

However, for intermediate pulse duration jets, some configurations were found where there was a significant overall out-flow of lateral jet energy, and with associated lateral jet mass out-flow. While individual shocks traverse to the stand-off shock rapidly, the flow configuration is significantly altered when a pulse endures so that the entire interface has time to reshape. Significant coherent pressure waves are then emitted into the adjacent ambient. Specifically, intermediate pulse duration jets with a low jet/ambient density-ratio and for higher jet/ambient overpressures lead to significant lateral energy out-flows (up to about 30 per cent of jet power).

The enhanced lateral energy out-flow jets had Mach disc stand-off shocks with large axial cyclic variations e.g. up to about 15 Rjet, which acted like bellows, driving out lateral jet pressure waves in the form of a series of ripples or bows.

In detail, the enhanced lateral power out-flow jets were associated with pulse duration greater than the dynamical time, and greater than, but comparable to, the Kelvin–Helmholtz jet surface wave crossing time to the stand-off Mach disc shock.

Key findings are summarized below: (i) Most pulsed jet configurations drive out the adjacent ambient along with the jet leading to an advected net in-flow of ambient energy/mass laterally toward the jet axis, i.e. setting up a convection pattern. (ii) Short-duration pulsed jets, with weak/oblique shock structures, generally tend to enhance lateral energy/mass jet in-flows. (iii) Long-duration pulsed jets temporarily transform to pseudo steady-state high Mach jets, with low-lateral jet energy/mass out-flows. (iv) Intermediate pulse duration jets with low-jet/ambient density-ratio and for higher jet/ambient overpressures lead to significant lateral energy out-flows (up to about 30 per cent of jet power). (v) The enhanced lateral energy out-flow jets had Mach disc stand-off shocks with large-axial cyclic variations e.g. up to about 15 Rjet, which acted like bellows, driving out lateral jet pressure waves. (vi) The enhanced lateral power out-flow jets were associated with pulse duration greater than the dynamical time, and greater than, but comparable to, the Kelvin–Helmholtz jet surface wave crossing time to the first/stand-off Mach disc shock.

Jet configurations with significant lateral energy out-flows identified here are sufficiently large to potentially match the energy budget needed to moderate galaxy cool-gas in-flows (Su et al. 2023). However, as well as the additional jet-physics needed, there remains questions over the extent and efficiency of energy transfer, as well as any potential for overheating.

We suspect that the dependence on Mach number is crucial and a systematic study of higher Mach number overpressured pulsed jets is needed to complement this Mach 2 study. Additional physics could include magnetic fields, relativistic gas, cooling and clumps, as well as winds, jet shear,and jet spray (Powell 1953; Massaglia et al. 2022). Energy transfer from bellows and ripples within a CGM with large density variations are also need to be considered. Also, the effects of a travelling energy burst along an overpressure jet may help understand observed travelling luminosity knots in some jets.

Further work will be needed to explore non-uniform CGM density profiles. Although lateral energy out-flows of ~ 30 per cent+ from higher power jets are sufficient to moderate galaxy cool-gas in-flows, further questions remain to be answered e.g. how efficiently is the energy transferred across the entire CGM? Can lateral mass out-flows also explain detected CGM metallicity? What characteristics may be identified which could be used as observational diagnostics?

DATA AVAILABILITY

No new observational data were generated or analysed in support of this research. Simulation source files are available on request. The data underlying this article will be shared on reasonable request to the corresponding author.

Underlying 1000-frame movies of a selection of simulations are available in the Zenodo repository, at https://zenodo.org/records/11078517 or through DOI: 10.5281/zenodo.11078517.

REFERENCES

Bambic C. J., Reynolds C. S., 2019, ApJ, 886, 78
Bonito R., Orlando S., Miceli M., Peres G., Micela G., Favata F., 2011, ApJ, 737, 54
Bourne M. A., Sijacki D., 2021, MNRAS, 506, 488
Chavan K., Dabhade P., Saikia D., 2023, MNRAS, 525, L87
Chen Y.-H., Heinz S., Enßlin T. A., 2019, MNRAS, 489, 1939
Donohoe J., Smith M. D., 2016, MNRAS, 458, 558
Duan X., Guo F., 2018, ApJ, 861, 106
Ehlert K., Weinberger R., Pfrommer C., Pakmor R., Springel V., 2018, MNRAS, 481, 2878
Fabian A., Sanders J., Allen S., Crawford C., Iwasawa K., Johnstone R., Schmidt R., Taylor G., 2003, MNRAS, 344, L43
Favata F., Bonito R., Micela G., Fridlund M., Orlando S., Sciortino S., Peres G., 2006, A&A, 450, L17
Franquet E., Perrier V., Gibout S., Bruel P., 2015, Prog. Aerosp. Sci., 77, 25
Gatuzz E. et al., 2023a, MNRAS, 525, 6394
Gatuzz E. et al., 2023b, MNRAS, 526, 396
Gómez J., Martí J. M., Marscher A., Ibáñez J. M., Alberdi A., 1997, ApJ, 482, L33
Guo F., Oh S. P., Ruszkowski M., 2008, ApJ, 688, 859
Hardcastle M., Krause M. G., 2013, MNRAS, 430, 174
Hillel S., Soker N., 2017, MNRAS, 466, L39
Huško F., Lacey C. G., 2023, MNRAS, 521, 4375
Ishibashi W., Fabian A., 2012, MNRAS, 000, 1
Jhan K.-S., Lee C.-F., 2016, ApJ, 816, 32
Martí J.-M., 2015, MNRAS, 452, 3106
Martí J. M., Perucho M., Gómez J. L., 2016, ApJ, 831, 163
Massaglia S., Bodo G., Rossi P., Capetti A., Mignone A., 2022, A&A, 659, A139
Mignone A., Bodo G., Massaglia S., Matsakos T., Tesileanu O., Zanni C., Ferrari A., 2007, ApJS, 170, 228
Mizuno Y., Gómez J. L., Nishikawa K.-I., Meli A., Hardee P. E., Rezzolla L., 2015, ApJ, 809, 38
Moya-Torregrosa I., Fuentes A., Martí J., Gómez J., Perucho M., 2021, A&A, 650, A60
Noriega-Crespo A., Raga A. C., Lora V., Rodríguez-Ramírez J. C., 2020, Rev. Mex. Astron. Astrophys., 56, 29
Peeples M. S. et al., 2019, BAAS, 51, 368
Perucho M., Quilis V., Martí J.-M., 2011, ApJ, 743, 42
Pfrommer C., 2013, ApJ, 779, 10
Porth O., Komissarov S. S., 2015, MNRAS, 452, 1089
Powell A., 1953, Proc. Phys. Soc. B, 66, 1039
Prasad D., Voit G. M., O'Shea B. W., 2022, ApJ, 932, 18
Roychowdhury A., Meyer E. T., Georganopoulos M., Kollmann K., 2023, MNRAS, 527, 10262
Ruszkowski M., Yang H.-Y. K., Reynolds C. S., 2017, ApJ, 844, 13
Sanders J. S., Fabian A. C., 2007, MNRAS, 381, 1381
Sanders J. S., Fabian A. C., 2008, MNRAS, 390, L93
Schoenmakers A. P., de Bruyn A. G., Röttgering H. J. A., van der Laan H., Kaiser C. R., 2000, MNRAS, 315, 371
Shabala S. S., Jurlin N., Morganti R., Brienza M., Hardcastle M. J., Godfrey L. E. H., Krause M. G. H., Turner R. J., 2020, MNRAS, 496, 1706
Shulevski A. et al., 2015, A&A, 579, A27
Smith M. D., 1982, ApJ, 259, 522
Smith M. D., Keogh T. L., 2022, MNRAS, 516, 2757
Smith M. D., Richards C., 2023, MNRAS, 526, 3407
Su K.-Y. et al., 2023, MNRAS, 000, 1
Tam C. K. W., 1995, Annu. Rev. Fluid Mech., 27, 17
Toro E. F., Spruce M., Speares W., 1994, Shock Waves, 4, 25
Walg S., Achterberg A., Markoff S., Keppens R., Porth O., 2014, MNRAS, 439, 3969
Weaver Z. R. et al., 2022, ApJS, 260, 12
Wong T. Y. M., Stavropoulos M. N., Beekman J. R., Towne A., Nogueira P. A. S., Weightman J., Edgington-Mitchell D., 2023, J. Fluid Mech., 964, A2
Yang H.-Y. K., Reynolds C. S., 2016, ApJ, 829, 90

APPENDIX A: LATERAL ENERGY AND MASS FLOWS

This section summaries the overall results of lateral energy and mass jet flows for the four base steady-state/constant in-flow jets. It also summaries the lateral energy flows for the pulsed simulations carried out. The results of further pulsed jet simulations are also summarized, where investigations were carried out, after significant lateral energy out-flows were discovered in low jet/ambient density jets with higher jet/ambient pressure ratios.

Table A1. Lateral energy and mass flow rates for the four constant in-flow jets. These are average rates between the time of 100 and 200 $R_{\rm jet}/c_{\rm amb}$. The normalized mass and energy units are based on the initial ambient density of 1. Note that the high-jet/ambient density ratio jets have much lower powers, due to their lower absolute speeds, and therefore lateral power in-flows can be a relatively high percentage of jet power. The negative lateral mass flow rates yet positive rates through the computational cylinder end-cap attests to the advection of ambient gas.

Simulation jet density ratio η	Simulation overpressure κ	Simulation designation	Lateral power	Jet power	Lateral mass out-flow	Jet mass out-flow	End-cap mass out-flow	Lateral/jet energy flow	Lateral/jet mass flow
0.1	2	M2K2E0.1R10	0.602	175.05	−0.736	2.634	1.388	0.34 per cent	−27.9 per cent
0.1	8	M2K8E0.1R10	3.216	1135.36	−20.10	5.440	11.70	0.29 per cent	−369.6 per cent
10	2	M2K2E10R10	−9.591	20.25	−6.406	27.00	6.429	−47.4 per cent	−23.7 per cent
10	8	M2K8E10R10	−30.012	136.80	−20.34	55.05	19.15	−21.9 per cent	−36.9 per cent

Table A2. Lateral powers for various pulse jets. Note significant lateral power out-flows for M2K8E0.1R10, P10V1.4, P10V2.0, and P40V2.0. Also, note large percentage power in-flows for M2K2E10R10P10V2.0, P40V1.4, and P40V2.0 due to very low-jet powers (high-density ratio jets have much lower absolute velocities).

	Lateral power/	% Lateral power/
Simulation	Jet power ratio	Jet power
M2K2E0.1R10P2V1.4	+11.7/133.1	+8.8
M2K2E0.1R10P2V2.0	−14.9/138.9	−10.7
M2K2E0.1R10P10V1.4	−5.5/166.6	−3.2
M2K2E0.1R10P10V2.0	−11.2/195.1	−5.7
M2K2E0.1R10P40V1.4	0.0/173.7	0.0
M2K2E0.1R10P40V2.0	+9.3/252.1	+3.7
M2K2E10R10P2V1.4	−7.5/18.1	−41.4
M2K2E10R10P2V2.0	−8.3/28.7	−28.9
M2K2E10R10P10V1.4	−14.9/18.6	−80.1
M2K2E10R10P10V2.0	−28.8/21.1	−136.5
M2K2E10R10P40V1.4	−21.7/16.1	−134.8
M2K2E10R10P40V2.0	−28.1/19.1	−147.1
M2K8E0.1R10P2V1.4	+23.0/623.2	+3.7
M2K8E0.1R10P2V2.0	−237.2/1209.5	−19.6
M2K8E0.1R10P10V1.4	+217.2/785.0	+27.7
M2K8E0.1R10P10V2.0	+409.1/1419.8	+28.8
M2K8E0.1R10P40V1.4	+59.9/1216.0	+4.9
M2K8E0.1R10P40V2.0	+451.1/2254.4	+20.0
M2K8E10R10P2V1.4	−6.2/121.1	−5.1
M2K8E10R10P2V2.0	−31.2/193.8	−16.1
M2K8E10R10P10V1.4	−54.5/84.0	−64.9
M2K8E10R10P10V2.0	−161.9/118.4	−136.7
M2K8E10R10P40V1.4	−32.6/110.8	−29.4
M2K8E10R10P40V2.0	+12.5/130.0	+9.6

Table A3. Lateral powers for low-jet/ambient density pulse jets, exploring further higher jet/ambient pressure ratios. Note significant lateral power out-flows for higher jet/ambient pressure ratio jets; $\eta = 0.1$ and $\kappa > 2$. Also note peak lateral power out-flows for intermediate pressure ratio, intermediate pulse duration jets.

e Simulation	Lateral power/ jet power ratio	Percent lateral power/ jet power
M2K3E0.1R10P2V1.4	−4.2/245.9	−1.7
M2K3.5E0.1R10P2V1.4	−7.3/172.7	−4.2
M2K3.5E0.1R10P2V2.0	−111.1/323.8	−34.3
M2K3.5E0.1R10P10V2.0	+41.2/300.9	+13.7
M2K3.5E0.1R10P40V2.0	+52.9/628.9	+8.4
M2K4E0.1R10P2V1.4	−6.1/322.9	−1.9
M2K4E0.1R10P2V2.0	−49.6/366.0	−13.6
M2K4E0.1R10P10V2.0	+97.4/401.6	+24.3
M2K4E0.1R10P40V2.0	+96.5/713.7	+13.5
M2K6E0.1R10P2V1.4	+40.1/391.7	+10.2
M2K6E0.1R10P2V2.0	−230.7/777.2	−29.7
M2K6E0.1R10P10V2.0	+293.2/905.0	+32.4
M2K6E0.1R10P40V2.0	+254.4/1398.7	+18.2

APPENDIX B: HEATING OF A COOLING AMBIENT MEDIUM

The energy lost from a jet to the ambient medium per unit time, $\dot{E}$, through a cylindrical surface of radius 13.5 $R_{\rm jet}$ and length 30 $R_{\rm jet}$, can be written in terms of the ambient parameters and the three jet parameters, η, κ, and Mach number M. We take an average fraction of kinetic jet power lost in the final half of these long duration simulations as calculated in this work, to be χ.

Hence $\dot{E} \sim \chi \dot{E}_{\rm jet} = \chi(0.5\pi R_{\rm jet}^2 \rho_{\rm jet} v_{\rm jet}^3)$. This yields

$$\dot{E} = 0.5\chi R_{\rm jet}^2 \rho_{\rm amb} c_{\rm amb}^3 \eta^{-1/2} \kappa^{3/2} M^3. \quad \text{(B1)}$$

This power fuels a region which we assume extends to a volume of $(25 \times 25 \times 30)\pi R_{\rm jet}^3$. Hence, the time-scale to double the energy contained in this region is approximately:

$$t_{\rm heat} \sim 4 \times 10^4 \chi^{-1} \eta^{1/2} \kappa^{-3/2} M^{-3}. \quad \text{(B2)}$$

Thus, the jet can theoretically moderate the cooling flow without it collapsing provided the cooling time exceeds this. If the cooling time of the CGM is 4 Gyr based on a scale of $30 R_{\rm jet} = 100$ kpc and $c_{\rm amb} = 1000\ {\rm km\ s^{-1}}$, then $t_{\rm cool} \sim 4,000 R_{\rm jet}/c_{\rm amb}$

Bearing in mind these very uncertain numbers, we then require

$$\chi \kappa^{3/2} M^3 > \eta^{1/2}, \quad \text{(B3)}$$

which is well satisfied in the case of low-density jets with the parameters studied here and χ of order 0.1

This paper has been typeset from a TEX/LATEX file prepared by the author.